Triboelectric nanogenerators for blue energy harvesting: Automated characterization and applicability studies

Marco Ramos
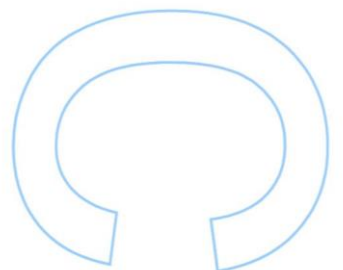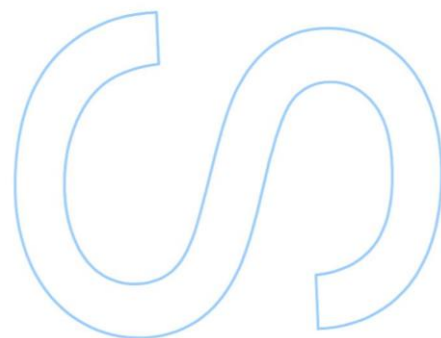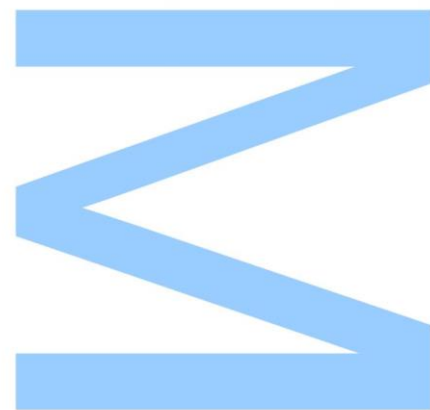
Mestrado Integrado em Engenharia Física
Departamento de Física e Astronomia
2020

Orientador
Prof. Dr. João Ventura, Investigador Principal,
Faculdade de Ciências da Universidade do Porto

Coorientador
Prof. Dr. Cândido Duarte, Professor Auxiliar,
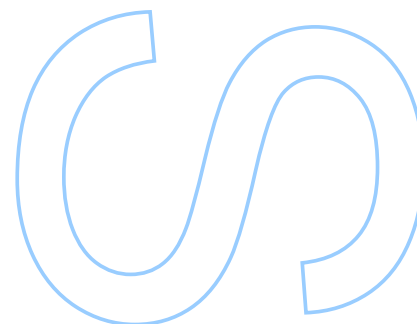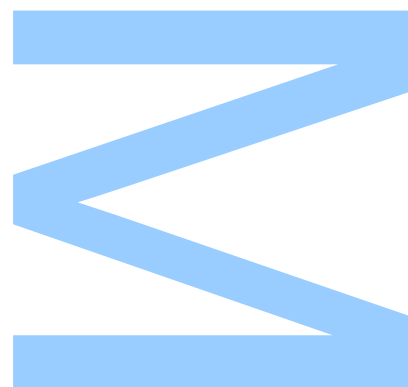Faculdade de Engenharia da Universidade do Porto

U. PORTO

FACULDADE DE CIÊNCIAS
UNIVERSIDADE DO PORTO

Todas as correções determinadas

pelo júri, e só essas, foram efetuadas.

O Presidente do Júri,

Porto, 09 / 10 / 2020

UNIVERSIDADE DO PORTO

MASTERS THESIS

Triboelectric nanogenerators for blue energy harvesting: Automated characterization and applicability studies

Author:

Marco RAMOS

Supervisor:

João VENTURA

Co-supervisor:

Cândido DUARTE

A thesis submitted in fulfilment of the requirements

for the degree of MSc. Engineering Physics

at the

Faculdade de Ciências da Universidade do Porto

Departamento de Física e Astronomia

October 8, 2020

*" Obstacles don't have to stop you. If you run into a wall, don't turn around and give up.
Figure out how to climb it, go through it, or work around it. "*

Michael Jordan

Acknowledgements

UNIVERSIDADE DO PORTO

Abstract

Faculdade de Ciências da Universidade do Porto

Departamento de Física e Astronomia

MSc. Engineering Physics

Triboelectric nanogenerators for blue energy harvesting: Automated characterization and applicability studies

by Marco RAMOS

With the increasing demand for energy and for different sources of energy as alternatives for fossil fuel, innovative technologies are being studied for specific types of energy needs. The triboelectric nanogenerator (TENG) is an energy harvesting device that converts mechanical into electrical energy, using a combination of the triboelectric effect and of electrostatic induction. This type of device is highly considered as an emerging technological advancement for offshore structures or wireless sensor network systems. These type of structures need power for their sensors, communication or data collecting. The TENG used in these structure can harvest energy from the slow motion of waves, for which TENGs have a large conversion efficiency. Also, the main advantages compared with other harvesters is the non dependency in conditions like the wind or the sun, and with this continuous energy harvesting comes other advantages like the low cost, low weight, low environmental impact and scalability for large scale projects.

In this dissertation, the first goal was the development of a software tool to help the processing of data acquired from TENGs, discovering pseudo periodic maximum data points fully automatically and outputting important plots and informations for the characterization of TENGs. After this was accomplished, two systems were built for different TENG characterization experimental tests. The first system studied the optimal load resistance by measuring voltage and current for different values of load resistance, and after that observe how the power depends on the load resistance.

Also, the first system allowed us to study the dependency of the amplitude and period of the motion on the TENG output, by varying these two values and plotting their

output in a 3 axis plot. With the second system, we studied how the TENGs reduced its output through time, with an experimental test that allowed 12 days of continuous and simultaneous measurement of three TENGs. After the 12 days of testing, it was possible to understand the time-dependence of the output voltage of the three different TENGs.

UNIVERSIDADE DO PORTO

Resumo

Faculdade de Ciências da Universidade do Porto

Departamento de Física e Astronomia

Mestrado Integrado em Engenharia Física

Nanogeradores triboelétricos como coletores de energia azul : Caracterização automática e estudos da sua aplicabilidade

por Marco RAMOS

Com a crescente procura por energia e por diferentes fontes de energia em alternativa aos combustíveis fósseis, tecnologias inovadoras estão a ser estudadas para necessidades específicas de energéticas. O nanogerador triboelétrico (TENG) é um dispositivo de captação de energia que converte energia mecânica em elétrica, utilizando uma combinação do efeito triboelétrico e da indução eletrostática. Este tipo de dispositivo é altamente considerado como um avanço tecnológico emergente para estruturas offshore ou sistemas de rede de sensores sem fio. Estes tipos de estruturas precisam de energia para os seus sensores, para comunicação ou para colheita de dados. O TENG utilizado nestas estruturas pode captar energia através movimento lento das ondas, para os quais os TENGs possuem uma grande eficiência de conversão. Além disso, as principais vantagens em comparação a outros tipos de colheita de energia é a independência de condições como o vento ou o sol, e com essa captação contínua de energia vêm outras vantagens como o baixo custo, baixo peso, baixo impacto ambiental e escalabilidade para projetos de grande escala.

Nesta dissertação, o primeiro objetivo foi o desenvolvimento de uma ferramenta de software para auxiliar o processamento dos dados adquiridos dos TENGs, descobrindo pontos máximos pseudoperiódicos de dados de forma totalmente automática e gerando gráficos e informações importantes para a caracterização dos TENGs. Com isto, dois sistemas foram construídos para diferentes testes experimentais de caracterização de TENG. O primeiro sistema estudou a resistência ótima de carga medindo a tensão e a corrente para diferentes valores de resistência de carga, e depois observou como é que a potência depende da resistência de carga.

Além disso, o primeiro sistema permitiu-nos estudar a dependência da amplitude e do período do movimento do TENG, variando esses dois valores e fazendo gráficos com o seu resultado num gráfico de 3 eixos. Com o segundo sistema, estudamos como os TENGs reduziram a sua potência ao longo do tempo, com um teste experimental que durou 12 dias, medindo continuamente e simultaneamente três TENGs. Depois dos 12 dias de testes, foi possível entender a dependência da tensão de saída dos três diferentes TENGs ao longo do tempo.

Contents

List of Figures

List of Tables

Chapter 1

Introduction

Today, we see multiple events that show how our environment and climate are changing. This is due to the fact that most energy generated today comes from fossil fuels like coal and natural gas, releasing harmful gases to the atmosphere and damaging our climate even more [1]. An alternative to fossil fuel use is by generating energy with renewable resources, which are not harmful to the environment.

Today, emerging technological advancements are increasing the demand for energy generation on offshore structures, for example, with Autonomous Underwater Vehicles (AUV) [2], wireless sensor networks for oceanographic research [3] or even for weather forecasting with sensor networks systems [4]. These type of structures need electrical power on their systems used for sensors, communication or even for data collecting. Typically, this electrical power is harvested with solar panels or small wind turbines, accompanied by batteries to store this energy. Although these methods are well-known, they have disadvantages. For example, solar panels only harvest energy during some hours of the day and wind turbines depend on the wind conditions. Unlike these last methods, in this dissertation, an alternative method will be presented for energy harvesting on offshore structures: the triboelectric nanogenerator (TENG).

The triboelectric nanogenerator is an energy harvesting device, converting mechanical into electrical energy, making use of the triboeletric effect and electrostatic induction [5]. The mechanical energy needed can come from multiples origins, like human motion [6], water motion [7] or even ocean waves [8]. The latter is the most important for this work, because TENG's are used to harvest energy from ocean waves, aiming to supply energy to offshore structures. These are very promising, due to their efficiency with irregular and low frequency ($<$5 Hz) waves [9], opposed from the traditional devices that use

electromagnetic generators, which are inefficient in these conditions [10]. Another reason why TENGs are so interesting and promising is because of their low cost, low weight, low density, low environmental impact and scalability for large scale projects.

This dissertation will be divided into six chapters, with this introductory chapter presenting a general view of TENGs and the motivation to research this type of devices. In Chapter 2, the general theory and characteristics of TENGs will be described. Also, the main modes of operation of TENGs and the most relevant configurations for ocean wave energy harvesting will be presented. Then, in Chapter 3, will be presented how the acquisition structure used in this dissertation was built and controlled for the study of the voltage and current output dependency on the load resistance, amplitude or period of the motion. Also, the software developed for data processing of TENGs will be presented and compared with an older and more time consuming method. In Chapter 4, the results obtained with the setup and software developed in Chapter 3 will be presented and discussed. Chapter 5 will present a new system developed to understand how the output of different TENGs decrease through time.

Finally, Chapter 6 presents the main conclusions of this work and shows an improvement of the system developed in Chapter 3, developing a system with 2 axis of rotations, increasing the realism of the ocean waves simulated. This system is still in development and can be optimised or even scaled up for larger or multiple TENGs.

Chapter 2

Triboelectric nanogenerators as ocean wave energy harvesting devices

2.1 Triboelectric effect

The triboelectric effect is known since Ancient Greece times, having the first mention of this phenomenon been attributed to the Ancient Greece philosopher, Thales of Miletus, who live somewhere between the 7th and 6th century B.C. He vaguely talked and spread the idea that amber would be attracted to other materials [11], having some other vague ideas for magnetism phenomenons and always with a philosophical approach for them. These type of phenomenons that Thales of Miletus talked about, are the phenomenons we know from our daily lives. A simple and familiar example to everyone would be the rubbing of a standard pen with our wool/cotton coat. After rubbing, the pen is able to attract small pieces of paper. This rubbing action is where the word "tribo" arises from, coming from the greek $\tau\rho\iota\beta\omega$/tríbõ, meaning "to rub".

This effect is based on inducing electrification by contact. Normally this effect occurs between two different materials, that become electrically charged after contact. The generated charge can result from electrons, ions or even by charged (nano-)material transfers, which can happen when hard friction or pressure is applied [12]. Normally the materials that show a stronger triboelectrification are insulators (low conductivity), which makes these materials store the transferred charged, generating with this electrostatic charges [5].

It is currently believed that right after two different materials touch each other, there is a chemical bond created upon adhesion, which happens on the surfaces of the materials.

This adhesion will then make the charges go from one material to the other to balance the potential created by the separation [5]. Right after the detachment of the materials, there will be some bonded atoms that will keep extra electrons, and others that will give away electrons, generating triboelectric charges at the surfaces of these materials [5]. The direction the electrons motion depends on the polarity of the specific materials used. Due to this dynamic, we will be generating an AC current, which is not ideal for powering small electronics, having to build an extra component for the conversion of AC to DC current, which can be done with a diode bridge.

Sometimes the triboelectric effect is undesired, for example, if inside a car's gasoline tank, there is a possibility of different materials to generate this type of electrostatic charges, then there would be the possibility of a discharge to happen, causing an explosion. Another example where this effect can cause problems is on sensitive electronic components, where the slight change in voltage or current can originate the destruction of that electronic component.

Although it is vaguely and superficially known since Ancient Greece or even before that period, today the triboelectric effect is widely studied, but not yet fully comprehended. Thus, there is still the need to understand and research it even more.

2.2   Triboelectric Nanogenerators

A triboelectric nanogenerator (TENG) is an energy harvesting device that can convert mechanical into electrical energy, due to the triboelectric effect and electrostatic induction [5]. This device was invented by Zhong Lin Wang's team in 2012 [13], having at the time, achieved an area power density of 3.67 mW/m^2. Only a year later, in 2013, it was possible to achieve an area power density of 313 W/m^2, improving the original value by 5 orders of magnitude [14]. This improvement was due to several optimized variables on the TENG's way of operating and structure, for example, the used materials, surface characteristics and even the modes of operation.

The simplest example of a TENG (Figure 2.1) is formed with two distinct materials, one having a tendency to lose electrons and another to gain electrons. They will be put into contact and then separated, generating electrical energy by connecting the external mechanical energy introduced into the system. Then, for generating more power, this dynamic of contact and separation should be repeated, having with this an ideal motion frequency. The ideal frequency is another great and innovative aspect of the TENG, because

unlike the electromagnetic generator (EMG), the TENG will be more power efficient at low frequencies (<10 Hz) [5], being, because of this, the prime selection for low frequency energy harvesting, such as energy harvesting from ocean waves (blue energy). Others examples include body motion, powering passive sensors or self-powering micro/nano systems [5].

This technology, can achieve groundbreaking performances with devices that have low mass, low density, low cost, low environmental impact and can be fabricated with easily obtainable materials. Also, TENGs typically have a low current and high voltage output. On the other hand, energy harvesting devices like solar cells, have high current and low voltage outputs, making them ideal to join TENGs and create hybrid generators, using both systems simultaneously and achieving great and interesting results [15].
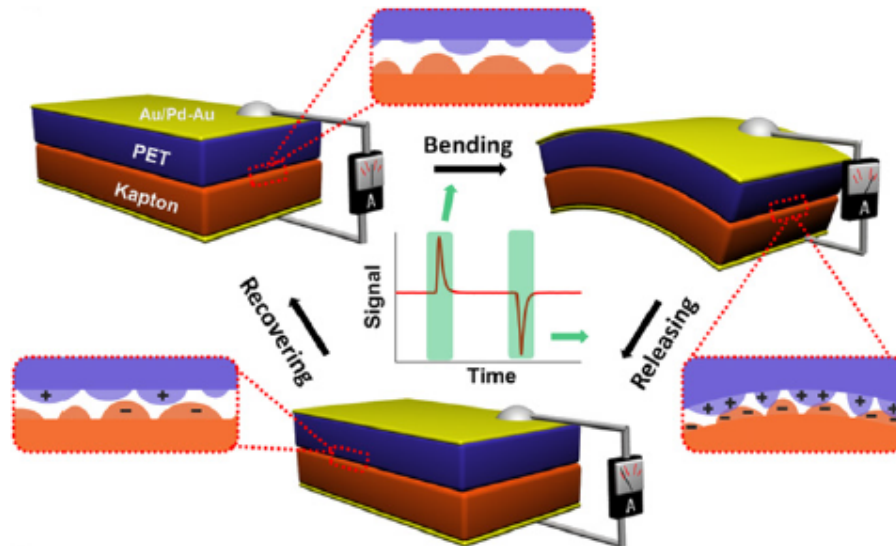
FIGURE 2.1: First TENG invented by Zhong Lin Wang's team in 2012 [13].

2.3 Triboelectric series

As said before, in this work, that some materials are more open to receive electrons, while others give electrons. In Figure 2.2 is shown the triboelectric series, where different types of materials can be observed, some more positively charged (lose electrons) and others more negatively charged (receive electrons) [16]. This propriety will be mostly dependent on the polarity of these different materials.

The different positions are a result of multiple variables, but generally, pairing a material at the top of the list with a material from the bottom will make a very good combination for a high performance TENG. These opposite materials will have an increasing amount of charges displaced and interchanged when the distance between the two, on the list, increases. Another important aspect of this list of materials, is that they are very affordable and easy to acquire or fabricate.

Some efforts were done with the goal of quantifying the triboelectric series [17], enabling the obtained values to be used on theoretical models, and increasing our knowledge about the triboelectric behaviour even more.
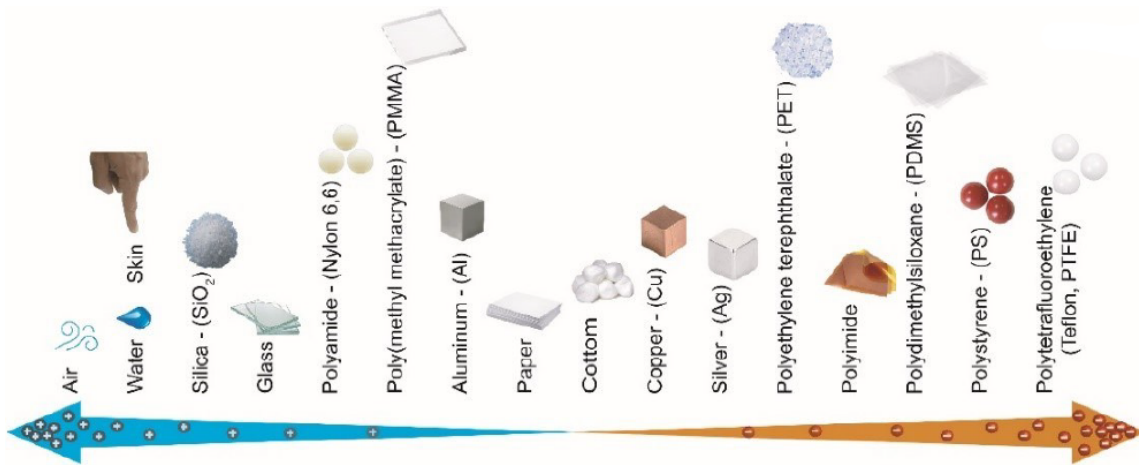
FIGURE 2.2: Triboelectric series with some of the most used materials in TENGs [18].

Although this series remains a good way to indicate how good a TENG will be with certain materials, there are exceptions to this series. These exceptions indicate two main results contradicting the triboelectric series, the cyclic triboelectric series and the triboelectrification of identical materials [12].

The first contradiction is the cyclic triboelectric series, as observed in Figure 2.3. This example is easy to understand; as the figure shows, from silk to zinc, each pair will behave as the triboelectric series indicates, one having the positive behaviour and another the negative. Finally, the combination of zinc with silk, the silk part will behave as the negative instead of positive, getting into a contradicting result [19].

The second contradiction is the tribo-electrification of identical materials, where it is suggested that identical materials can generate charge density, which although low, still confuse researchers on how it happends. Some studies indicate that this is due to the difference on each surface's roughness (nano-structures) and their curvature, having as the conclusion of their work, that positive curvature surfaces will generate negatively charged

FIGURE 2.3: Example of a cyclic triboelectric series [12].

surfaces and negative curvature surfaces will generate positively charged surfaces, holding with low pressure or even high temperature environments [20].

For both contradictions, there is still insufficient evidence to prove and support these two distinct hypothesis [12].

2.4 TENG's surface characteristics

A TENG can be optimized by different factors. One of those factors is the surface structure, that can be so important as to raise the power output by several orders of magnitude.

In Figure 2.4 it can be observed the difference on the output voltage and current of identical area TENGs but with different structure on their surfaces. These different surfaces were found to make a huge difference on the generated output power [21]. One way to understand this is thinking on the enlargement of the surface area that each structure accomplishes. On the case of the pyramids, the real surface area will be bigger compared with the normal surface, like the flat film example. This highly efficient TENG surface structures, can be used as self-powered pressure sensor sensing things like water droplets

with 8 mg and feathers with 20 mg, each with 3.6 Pa and 0.4 Pa contact pressure respectively, and having a minimum detection limit of about 13 mPa [21].
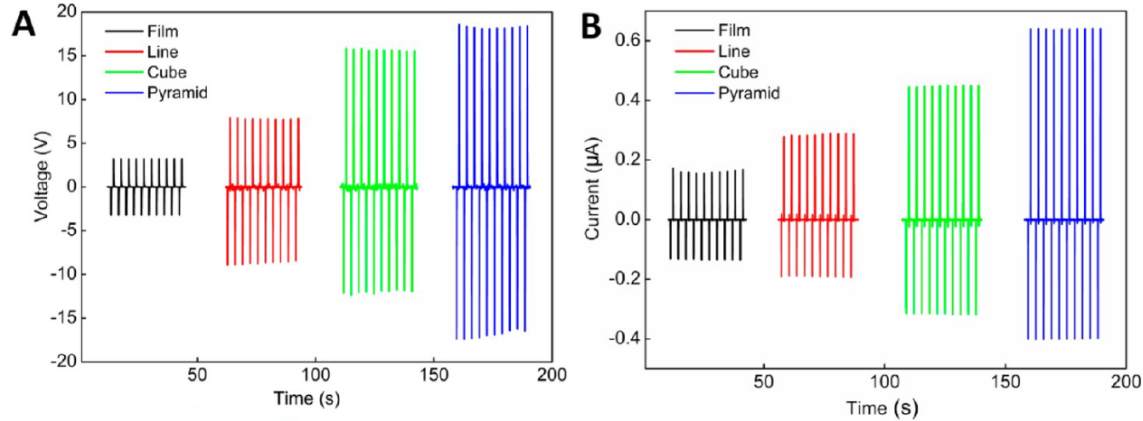
FIGURE 2.4: Output voltage and current of equal TENGs with different surfaces [21].

The change of the surface can come as a benefit regarding the power output, but in the long run, experiments show that some surface structures that are more effective on generating power, can be less durable. In Figure 2.5, an experiment can be observed where the current through time gets degraded faster on a "Dome" structure than on a "Pillar" structure. Between the two structures, the "Dome" structure, is the one that has larger outputs, due to the higher surface area, but this has a disadvantage, degrading faster due to the larger surface area and the way the structure reacts to friction and compression [22].
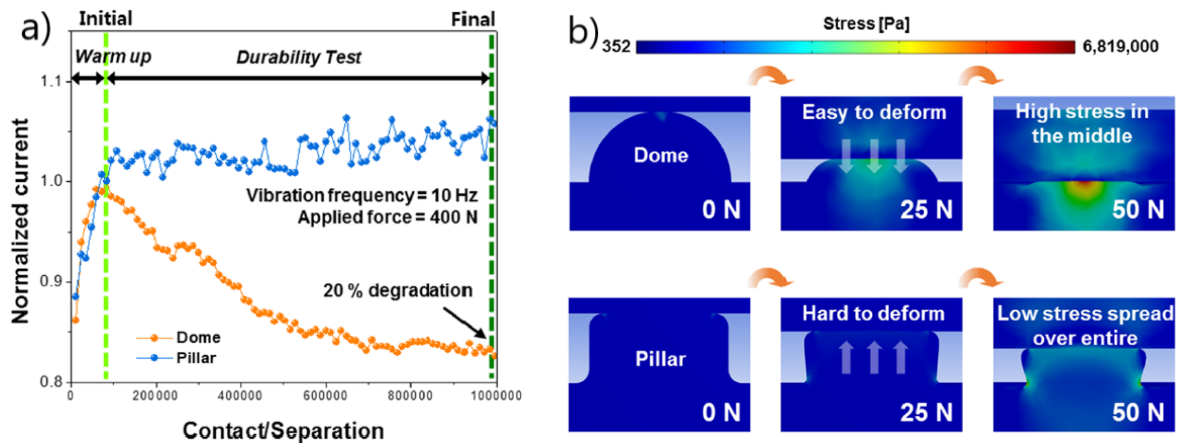
FIGURE 2.5: (a) Degradation of the 2 types of surface structure output's throughout time [22]. (b) The 2 types of surface structures [22].

2.5 Fundamental Theory of TENGs

The simplest TENG imagined, illustrated in Figure 2.6, should have two materials opposite to each other, the tribo-pairs, called Dielectric 1 and Dielectric 2, with relative dielectric constants ϵ_{r1} and ϵ_{r2}. These will be placed into contact with each other, having a variable distance (x) between the two opposite layers of the two materials, with opposite charges (tribo-charges densities $+\sigma$ and $-\sigma$) as a result from the contact electrification [23].

Apart from this, there will be two external electrodes, called Metal 1 and Metal 2, that will enable charges to flow on an external circuit. These charges will flow from an electrode to another, with a value Q, resulting on one electrode having -Q charge and the other electrode with +Q charge.
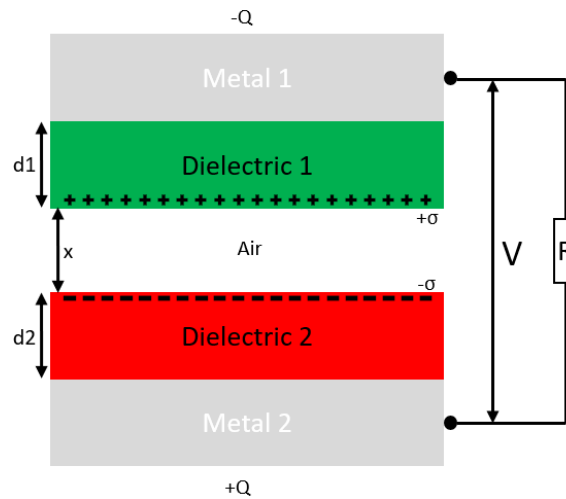
FIGURE 2.6: Basic TENG structure.

These two types of generated charges will be the two components of the electrical potential difference between the two electrodes on the TENG [24]. The first will come from the tribo-charges which are on the dielectric surfaces and are dependent on the distance between them. This component of the TENG's voltage is called open-circuit voltage ($V_{OC}(x)$). The second will come from the transferred charges between the two sections of the TENG. Without the tribo-charges, the TENG would be a capacitor, having equal opposite charges, generating an electrical potential equal to $-\frac{Q}{C(x)}$, where C is the capacitance, which has a dependency on the distance between the surfaces. The two components will have a total potential difference given by [23]:

$$V_{TENG} = -\frac{Q}{C(x)} + V_{OC}(x).$$

(2.1)

This last expression is called V-Q-x relationship, which is the main governing equation for TENGs, having a obviously dependency in their capacitive behaviour.

After this, an important fact to understand is that under short-circuit conditions, the transferred charges (Q_{SC}) will neutralize the tribo-charges created on the materials surfaces, easily showing that on a TENG, under short-circuit conditions, one obtains [23]:

$$0 = -\frac{Q_{SC}(x)}{C(x)} + V_{OC}(x). \tag{2.2}$$

Reorganizing the components of this relationship, we clearly see the relationship between Q_{SC}, C and V_{OC} [23]:

$$Q_{SC}(x) = C(x) \cdot V_{OC}(x). \tag{2.3}$$

This relationship will enable the possibility of achieving an equivalent circuit model for a TENG, composed by two circuit elements, one for each components of the V-Q-x relationship expression. The first will be the capacitive element of the circuit, which will be generated between the electrodes and will be represented by a capacitor C. The second element of the circuit will have an origin on the separation of the tribo-charges represented by an ideal voltage source, $V_{OC}(x)$ [23]. These two, due to the expression above, will be put on the equivalent circuit in a serial connection, like Figure 2.7 illustrates.
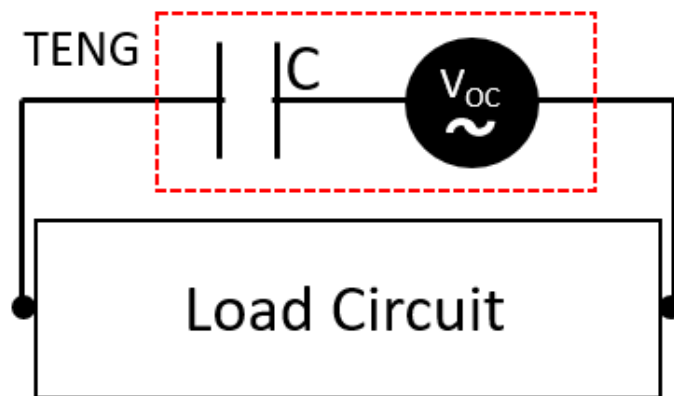
FIGURE 2.7: Basic TENG equivalent circuit.

Another important aspect to know about a TENG device is that its intrinsic impedance will come mainly from its intrinsic capacitance [24]. This is because a TENG will be designed to have very high values of resistance to optimize the power output, and also the metal parts of the TENG will have low resistance, being irrelevant for the total impedance.

Joining the fact that TENGs and traditional electromagnetic generators (EMGs) have totally different ways of generating power, the fact that TENGs are intrinsically capacitive, makes their internal resistance very high. On the other hand, EMGs are intrinsically resistive, which makes their internal impedance much lower than that of TENG's impedance. This results on TENGs and EMGs being high-resistance and low-resistance voltage sources, respectively. Although this does not look like an important fact, these two differences on generating power, can be combined on hybrid generators, that use both EMG and TENG for better output results [5].

2.5.1 Resistive Load characteristics

As seen above, an easy way to characterize a TENG is by a small capacitor and a voltage source, which can be connected to a arbitrary load on the circuit. This load will be a purely resistive load, making the calculations easier. Using Kirchhoff's law, we can derived the next equation for the whole system [24] :

$$R \cdot \frac{dQ}{dt} = -\frac{Q}{C(x)} + V_{OC}(x).$$
(2.4)

This differential equation, can be solved using complex numerical methods like the finite element method (FEM) [5], which is a general method used on every TENG design. Other methods exist and even specific software exists just for simulating TENG's behaviour.

The resistive load used on a TENG device can be optimized for the maximum power output. This is possible by measuring the output voltage and current of the TENG, on parallel and serial measurements on the load, respectively. Both of the acquisitions are needed because both values are to calculate the instantaneous power output of the TENG. This calculation is possible due to the combination of Joule's law ($P = I^2R$) and Ohm's law ($V = IR$), leading to :

$$P = V \cdot I.$$
(2.5)

This expression is then used to calculate the values of the instantaneous output power for every value of load resistance, acquiring a characteristic behaviour of the output power.

In Figure 2.8, we can see two different plots. The first shows the maximum values of current and voltage for different load resistances and the same motion applied to the TENG. The second shows the values of instantaneous power output with different load resistances. These results are theoretical but very close to the behaviour observed in experimental results [25].

In each of these plots, there are interesting facts to understand. On the first plot, we see three different regions marked. These are where the TENG enters different regimes. In "Region I", with small resistances, the current converges to the maximum value which is possible on short circuit (SC) conditions. On the opposite side, in "Region III" we see the resistance diverging, making the voltage achieve the maximum value, the open circuit (OC) conditions. On both of this regions, the other measured physical property is converging to a value of zero. Finally, in "Region II", we see the current decreasing rapidly and the voltage increasing rapidly; it is in this region that the maximum instantaneous output power will be reached (100 MΩ in this example) [25]. It is on the second plot, where this maximum value of the instantaneous maximum output power is visualized.
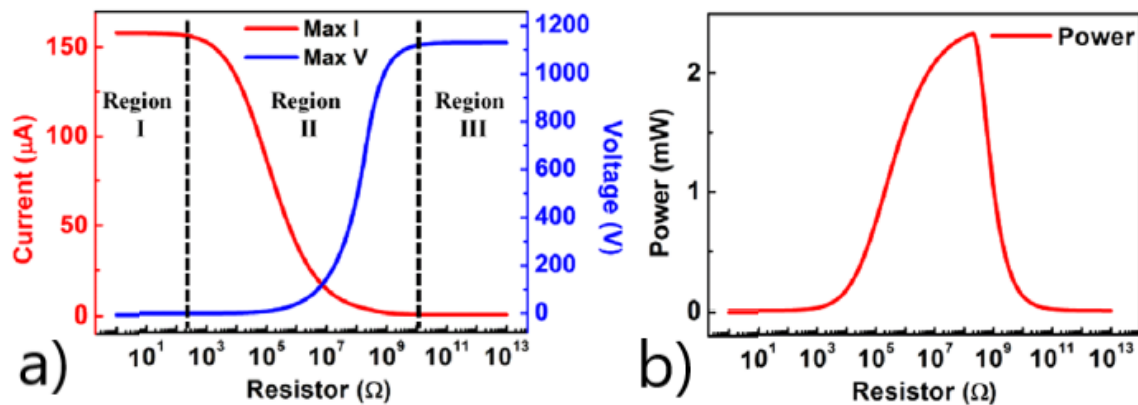
FIGURE 2.8: Theoretical outputs for different load resistance values used on a TENG under uniform velocity separation. (a) The dependency of load resistance on the output values of current and voltage and the three marked regions. (b) The dependency of the output values of the maximum instantaneous output power on the load resistance [25].

Other studies on the output values of TENGs can be done, including studies on the dependency of the frequency of the motion of the TENG, leading to interesting results and enabling new improvements in TENG designs [26].

2.6 TENG modes of operation

Triboelectric nanogenerators have four different modes of operation, making each mode unique for the generation of energy and different configurations of their components. These modes are the Vertical Contact-Separation Mode, the Lateral Sliding Mode, the Single-Electrode Mode and the Freestanding Triboelectric-Layer Mode [5]. Each one of these modes will be described below.

2.6.1 Vertical Contact-Separation Mode

The first ever used and most simple mode of a TENG is the Vertical Contact-Separation Mode, which produces power with contact and separation of two opposite surfaces, as seen on Figure 2.6. Apart from what was already explained, these two dielectric materials will have a thickness of d1 and d2, generating a potential difference between the electrodes when these are separated. When they go through this motion, there will be charge transferred between electrodes, achieving on the top electrode a total of -Q charge and the bottom electrode with +Q charge. On the surfaces of Dielectric 1 and Dielectric 2, there will be $+\sigma S$ and $-\sigma S$ charge respectively. This is the case where we have two dielectrics, called dielectric-to-dielectric mode type. Another type is the conductor-to-dielectric, which occurs when one of the dielectrics is replaced by a single conductor that plays both roles, as triboelectric and electrode layers [24]. This will result on this conductor having the sum of the Dielectric 1 and Metal 1 charges ($+\sigma S$ - Q). Due to the fact that the size of the electrodes is much larger than the separation between the electrodes ($d1 + d2 + x(t)$), we can consider this as an ideal capacitor enabling us to use the classical expression of a the capacitance of a capacitor as $\epsilon \frac{A}{d}$. Also, because of this assumption, the voltage between the two dielectrics (V_{OC}) will be $\frac{Q}{C} = \frac{Qd}{A\epsilon} = \frac{\sigma d}{\epsilon}$. Knowing these two, we can derive [23]:

$$V_{OC} = \frac{\sigma x(t)}{\epsilon_0}, \tag{2.6}$$

$$C = \frac{\epsilon_0 S}{d_0 + x(t)}, \tag{2.7}$$

$$d_0 = \frac{d1}{\epsilon_{r1}} + \frac{d2}{\epsilon_{r2}}, \tag{2.8}$$

$$V_{TENG} = -\frac{Q}{C} + V_{OC} = -\frac{Q(d_0 + x(t))}{\epsilon_0 S} + \frac{\sigma x(t)}{\epsilon_0}. \tag{2.9}$$

The last expression will be the V-Q-x relationship of the Vertical Contact-Separation Mode. Another value that can be extracted is the short circuit charge :

$$Q_{SC} = V_{OC} \cdot C = \frac{S\sigma x(t)}{d_0 + x(t)}. \tag{2.10}$$

In Figure 2.9 we see the output resulting from two different conditions for this mode. The first for I_{SC} in short-circuit and a second one for V_{OC} in open-circuit.

In the short-circuit condition, if the TENG is pressed, there will be charges going from one electrode to the other in one way, because of the electrical potential difference created by the triboelectric effect when the two surfaces come into contact. When the TENG is released out of contact, the opposite will occur, resulting on small periods of positive or negative current, depending on which one of the action occurs. If the motion stops either while in contact or not, the current will be neutralized [5].

On the open-circuit condition, when the two surfaces of the TENG come into contact, due to the triboelectric effect, there will be charges generated on the two surfaces, when these surfaces get separated, the voltage will increase rapidly, until the maximum distance is reached. When the two surfaces are pressed together, the voltage will decrease rapidly to the original value. These outputs are only possible to obtain with electrometers with very large input impedance [27] and with the initial position equal to the final position after releasing and pressing.
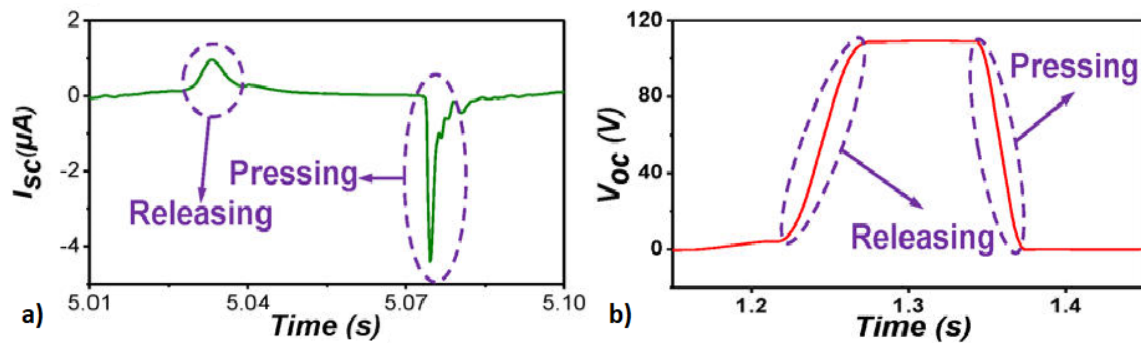
FIGURE 2.9: Example of the TENG output with different conditions [27]: (a) Short-circuit and (b) Open-circuit.

2.6.2   Lateral Sliding Mode

This second mode will be very similar to the Vertical Contact-Separation mode, but in this case the separation direction is parallel to the TENG's surface. When the two dielectric surface touch each other, by the triboelectric effect each one will have opposite charges on their surfaces, with equal charge densities. From the first mode, we know that, when these surfaces are together and their gap is zero, the electrical potential across the electrodes will be zero. When the sliding of the surfaces starts ("x" increasing), like Figure 2.10 shows, the charges that are left isolated, will generate an electric field. This electric fields will be on the y-direction (up and down) and will induce potential difference on the electrodes, driving a current flow on one direction, through the external load resistance. When the sliding comes back together ("x" decreasing), the opposite will occur and the current will flow back on the other direction, in order to preserve electrical equilibrium [28]. This working principle supposes, like the first mode, that the length or area of the dielectric surfaces is much larger that the corresponding thickness, neglecting edge effects, which are common problems in capacitor systems [5]. Also, as the first mode, the lateral sliding mode will have two general types, the dielectric-to-dielectric and conductor-to-dielectric. The difference, again, is the top section of Metal 1 and Dielectric 1 being replaced by a conducting Metal, making it exhibit the behaviour of both parts at the same time.
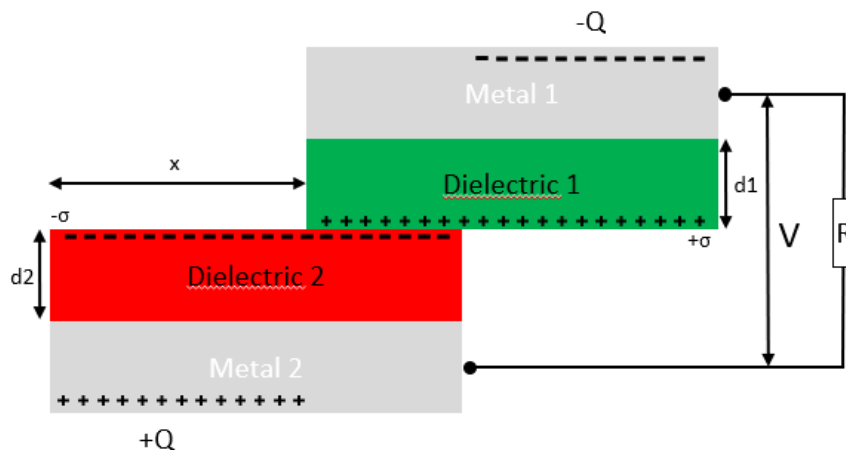
FIGURE 2.10: Lateral Sliding Mode structure.

As before, the transferred charge will be defined by Metal 1 with -Q transferred charge and Metal 2 with Q transferred charge. The sliding as said before, will leave some part on top of each other, and others isolated to each side, generating electric fields. The isolated parts will have σwx charge, with "w" for width, and with this, the top electrode (Metal 1)

will have the same amount of charge. The parts that touch on Dielectric 1 and Dielectric 2 will have σw(L-x), with L for the total length. This will be mirrored to the bottom section of the TENG. The V-Q-x relationship can be derived from these facts and, using the same supposition as the first mode, we get for the total capacitance [5]:

$$C = \frac{\epsilon_0 w(L - x)}{d_0}. \tag{2.11}$$

For the value of V_{OC}, we suppose that the plates are infinite. With this assumption, the charge distribution and the electric fields will be uniform. Because of this, we will have the following charge distribution in both electrodes [28]:

$$
\begin{aligned}
\rho &= \sigma & \text{, for the non-overlapped region of the bottom electrode} \\
\rho &= -\frac{\sigma x}{L - x} & \text{, for the overlapped region on the bottom electrode} \\
\rho &= -\sigma & \text{, for the non-overlapped region of the top electrode} \\
\rho &= \frac{\sigma x}{L - x} & \text{, for the overlapped region on the top electrode}
\end{aligned}
\tag{2.12}
$$

We then know from Gauss theorem, that we can get the electric field ($\frac{\rho}{\epsilon}$) on the overlapped regions, on Dielectric 1 and Dielectric 2 [28]:

$$E_1 = \frac{\sigma x}{\epsilon_0 \epsilon_{r1}(L - x)}, \tag{2.13}$$

$$E_2 = \frac{\sigma x}{\epsilon_0 \epsilon_{r2}(L - x)}. \tag{2.14}$$

Both electric fields will point to the negative y-direction. With this we can derive the expression for V_{OC} [28]:

$$V_{OC} = E_1 d_1 + E_2 d_2 = \frac{\sigma x}{\epsilon_0 (L - x)}(\frac{d_1}{\epsilon_{r1}} + \frac{d_2}{\epsilon_{r2}}) = \frac{\sigma x d_0}{\epsilon_0 (L - x)}. \tag{2.15}$$

Having the value of V_{OC}, the V-Q-x relationship can be derived for the lateral sliding mode :

$$V_{TENG} = -\frac{d_0}{w\epsilon_0 (L - x)}Q + \frac{\sigma x d_0}{\epsilon_0 (L - x)}. \tag{2.16}$$

Finally, the value for Q_{SC} will be define as:

$$Q_{SC} = V_{OC} \cdot C = \sigma w x. \tag{2.17}$$

2.6.3 Single-Electrode Mode

The third mode will have a lot of similarities with the other two modes, depending on if it is a structure in contact-separation or lateral sliding. In these two cases, the triboelectric pair will be composed by a dielectric surface and an electrode with the same area S (length L and width w), called Dielectric 1 and Primary Electrode (PE), respectively.

In Figure 2.11 we see the basic structure for a conductor-to-dielectric single-electrode mode TENG. The Reference Electrode (RE) can work as a ground, so that when the dielectric is separated from the PE charges originated from the triboelectric effect it will establish a potential difference between the two electrodes. If the two electrodes are in short circuit conditions, this will make charges flow from on electrode to the other. When the dielectric surfaces comes back into contact with the PE, these charges will go back to neutralize the potential difference created by the dielectric surface charges. In the case of open-circuit conditions, the voltage will increase to a maximum value when the dielectric layer is the farthest and a minimum when its in contact with the PE [5].
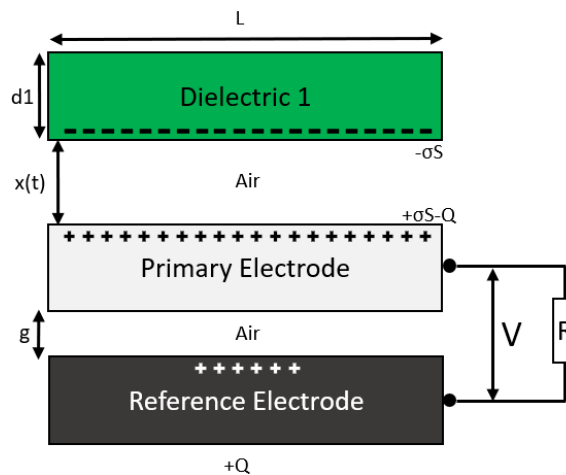
FIGURE 2.11: Single-Electrode Mode structure.

As before, Q will define the transferred charges between both electrodes, g will be the gap between these two electrodes, having a fixed value. Opposite to that is variable distance x(t), between Dielectric 1 and PE. At the first moment of contact, the Dielectric 1 and PE will have -σ and +σ surface charge density, respectively. Adding the charges from the transferred charges when the Dielectric 1 and PE get separated, the resulting total charge for the PE and RE is $\sigma S - Q$ and Q, respectively [5].

In order to understand how the V-Q-x relationship is derived for this mode, the corresponding equivalent circuit, needs to be understood. Figure 2.11 illustrates the equivalent

circuit of the Single-Electrode mode for a TENG. This figure shows that there are three capacitors, with different capacitances. Between these capacitor, there are three nodes corresponding to the dielectric surface, the PE and the RE, respectively.
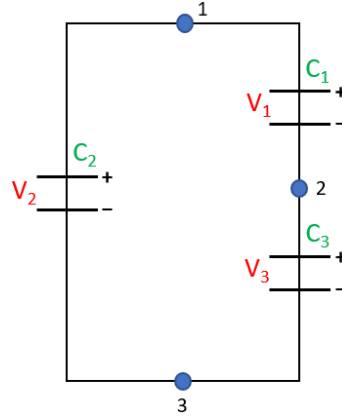
FIGURE 2.12: Single-Electrode Mode equivalent circuit [29].

The capacitance between Node 1 and Node 3 (C_b), will contain two parts, the C_2 in parallel with serial connection of C_1 and C_3, giving [29]:

$$C_b = C_2 + \frac{C_1 C_3}{C_1 + C_3}. \tag{2.18}$$

With the same practices, the capacitance between Node 1 and Node 2 (C_a) and between Node 2 and Node 3 (C_c) will be given by [29]:

$$C_a = C_1 + \frac{C_2 C_3}{C_2 + C_3}, \tag{2.19}$$

$$C_c = C_3 + \frac{C_1 C_2}{C_1 + C_2}. \tag{2.20}$$

Having these three expressions, it is possible to reach expressions for C_1, C_2 and C_3 depeding on C_a, C_b and C_c. If on the OC condition, the total charge on nodes 1, 2 or 3 will be -σS, - σS and 0. The following expressions can then be derived [29]:

$$V_2 = V_1 + V_3, \tag{2.21}$$

$$V_3 = V_{OC} = \frac{\sigma S C_2}{C_1 C_2 + C_2 C_3 + C_3 C_1}, \tag{2.22}$$

$$Q_{SC} = V_{OC} C_c = \frac{\sigma S C_2}{C_1 + C_2}. \tag{2.23}$$

2.6.4 Freestanding Triboelectric-Layer Mode

This last mode will have two sub-types, the sliding and the contact freestanding triboelectric-layer modes. Each one will be discussed separately.

2.6.4.1 Contact Freestanding Triboelectric-Layer Mode

In this mode there will be some variants, with some using a dielectric as the freestanding layer and others with two dielectrics on top and bottom of the TENG, and a third metal used as the freestanding layer in the middle.
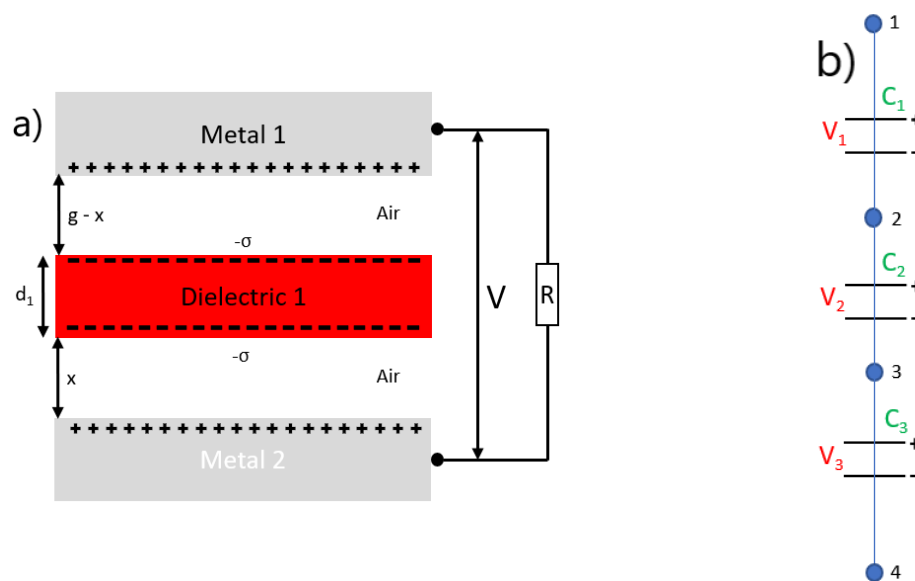
FIGURE 2.13:   (a) Contact Freestanding Triboelectric-Layer mode structure with a dielectric-freestanding-layer and (b) Equivalent circuit.

In Figure 2.13a, it is shown the structure of a dielectric-freestanding layer on a Contact Freestanding TENG. This layer will form two triboelectric pairs with the two metal plates around the layer. The distance between both metal plates will be defined by "g". After a contact with the plates, the dielectric surfaces will have charges due to the triboelectric effect. As always it is assumed that the charge density is uniform on the surfaces, and with this, the dielectric surfaces will have $-\sigma$ charge density, with the two metal plates having the same total charge but in this case being positive, due to charge conservation [5]. Also, the length and width will be considered much larger than the air gaps in between the plates and the dielectric, making the edge effects residual. The equivalent circuit model showed in Figure 2.13b will have four nodes, each one for each surface of Figure 2.13a, and three capacitors in series, giving a total capacitance [5]:

$$C = \frac{1}{\frac{1}{C_1} + \frac{1}{C_2} + \frac{1}{C_3}} = \frac{\epsilon_0 S}{d_0 + g}. \tag{2.24}$$

When in short circuit (SC) condition, nodes 1 and 4 will have the same potential. As said before, the charges on nodes 2 and 3 (dielectric surfaces), will be -σS. So, the same positive amount will be on nodes 1 and 4, with separated charges of Q_1 and Q_2 respectively, and a total value of 2σS. With this knowledge we can then derive [30]:

$$V_1 + V_2 + V_3 = 0, \tag{2.25}$$

$$V_1 = \frac{Q_1}{C_1}, \tag{2.26}$$

$$V_2 = -\frac{\sigma S - Q_1}{C_2}, \tag{2.27}$$

$$V_3 = -\frac{2\sigma S - Q_1}{C_3}. \tag{2.28}$$

This will make the values of Q_1 and Q_2 as [30]:

$$Q_1 = \sigma S \frac{\frac{1}{C_2} + \frac{2}{C_3}}{\frac{1}{C_1} + \frac{1}{C_2} + \frac{1}{C_3}}, \tag{2.29}$$

$$Q_2 = \sigma S \frac{\frac{2}{C_1} + \frac{1}{C_2}}{\frac{1}{C_1} + \frac{1}{C_2} + \frac{1}{C_3}}. \tag{2.30}$$

Due to the fact that C_2 will be much larger than d_1, the expressions of Q_1 and Q_2 can be simplified to:

$$Q_1 \approx \frac{2\sigma S}{1 + \frac{C_3}{C_1}}, \tag{2.31}$$

$$Q_2 \approx \frac{2\sigma S}{1 + \frac{C_1}{C_3}}. \tag{2.32}$$

These last two expressions will enable the understating of the mechanism of the TENG mode. For example, when x tends to zero, C_3 will tend to infinity, making the value of Q_1 and Q_2 tend to zero and 2σS, respectively. On the other hand, when x tends to g, C_1 will tend to infinity, making the value of Q_1 and Q_2 tend to 2σS and zero, respectively. This two similar mechanisms on each side of the TENG, will make the current flow from

one side to the other, alternating when the position of the dielectric changes. Finally, the values of the Q_{SC} and V_{OC} will be given by [30]:

$$Q_{SC} = \frac{2\sigma S x}{d_0 + g},\tag{2.33}$$

$$V_{OC} = \frac{Q_{SC}}{C} = \frac{2\sigma x}{\epsilon_0}.\tag{2.34}$$

With the last two equations, the V-Q-x relationship can be derived as [30]:

$$V_{TENG} = -\frac{Q}{C} + V_{OC} = -\frac{d_0 + g}{\epsilon_0 S}Q + \frac{2\sigma x}{\epsilon_0}.\tag{2.35}$$

2.6.4.2   Sliding Freestanding Triboelectric-Layer Mode

As the contact type of the freestanding triboelectric-layer mode, this type will have a variant with only a dielectric freestanding triboelectric-layer and another with a metal layer above the dielectric one. In Figure 2.14 we can see the illustration of the structure of the first variant. As it is shown, g will be the separation between the metal layers and h the separation between the metal layers and the freestanding dielectric layer.
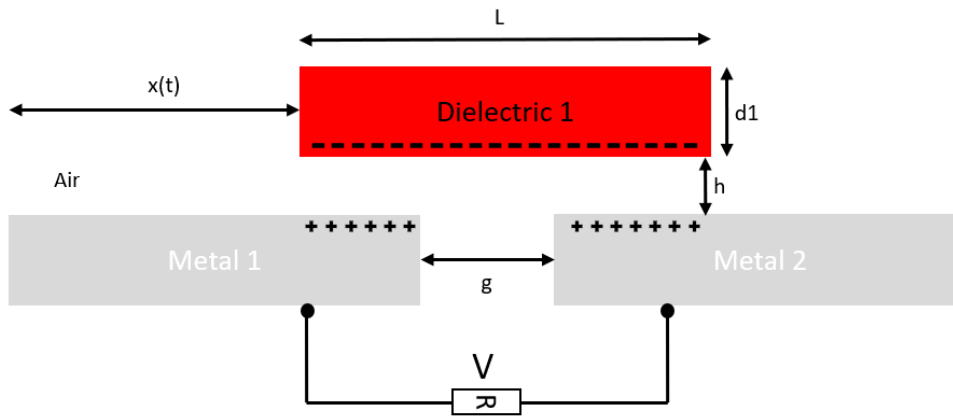
FIGURE 2.14: Sliding Freestanding Triboelectric-Layer mode structure with a dielectric-freestanding-layer.

As seen on the contact type, the node concept is used to reach an equivalent circuit. This time however, the electrical potential on the bottom dielectric will not be a constant, and will not be seen as a unique node [30]. First, it is assumed that a small region of "dk" at the bottom dielectric surface will have the tribo-charges with a density of σ, with the total charges on metals 1 and 2 being σwdk. So, in SC conditions, one has [30]:

$$dQ_1 = \frac{\sigma wdk}{1 + \frac{C_2(k)}{C_1(k)}}, \tag{2.36}$$

$$dQ_2 = \frac{\sigma wdk}{1 + \frac{C_1(k)}{C_2(k)}}. \tag{2.37}$$

C_i(k) will be the capacitances between the small surface σwdk and metal i. This will enable us to achieve the values for the total charges on metals 1 and 2, by integrating each tribo-charged region [30]:

$$Q_1 = \sigma w \int_0^L \frac{dk}{1 + \frac{C_2(k)}{C_1(k)}}, \tag{2.38}$$

$$Q_2 = \sigma w \int_0^L \frac{dk}{1 + \frac{C_1(k)}{C_2(k)}}. \tag{2.39}$$

This results on a total charge, for a complete movement from zero to g+L on SC condition [30], given by:

$$Q_{SC} = \int_0^L \frac{\sigma wdk}{1 + \frac{C_2(k)}{C_1(k)}\Big|_{x=g+L}} - \int_0^L \frac{\sigma wdk}{1 + \frac{C_2(k)}{C_1(k)}\Big|_{x=0}}. \tag{2.40}$$

Obviously, when x=0, Q_1 and Q_2 will be σwL and zero, respectively. When x=g+L, the opposite occurs. These values enable Q_{SC} to reach σwL, achieving charge efficiencies of 100%.

2.7 TENG applications for ocean wave energy harvesting

As it was said already in this work, triboelectric nanogenerators are a powerful and efficient tool to harvest energy from ocean waves, since these waves, most of the times, have very low frequencies (<1 Hz). Ocean waves are normally characterized by their frequency and amplitude. On the other hand, ocean floating devices used terms like surge, sway and heave for linear movements and roll, pitch and yaw for rotation movements on the x, y and z axis, respectively (Figure 2.15).

Regarding TENG's applications for ocean wave energy harvesting, there are multiple examples, but here, only the most relevant and similar to the ones developed in this dissertation will be detailed.
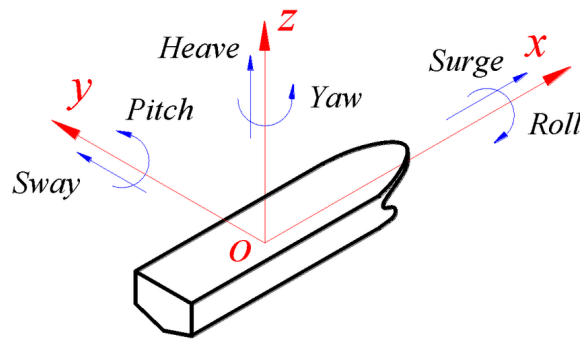
FIGURE 2.15: Movements done by an oceanic floating body [31].

The first example is a tower-like TENG (T-TENG) that has multiple units inside (Figure 2.16 (a)). These are made with an arc surface structure, PTFE balls rolling above Nylon films with a bottom metal electrode. The complete structure with multiple units increased its power output linearly with the number of units. One of this unit (Figure 2.16 (b)) was able to generate 1.03 W/m^3 [32]. This design is very good and has the same output for equal pitch and roll movements.
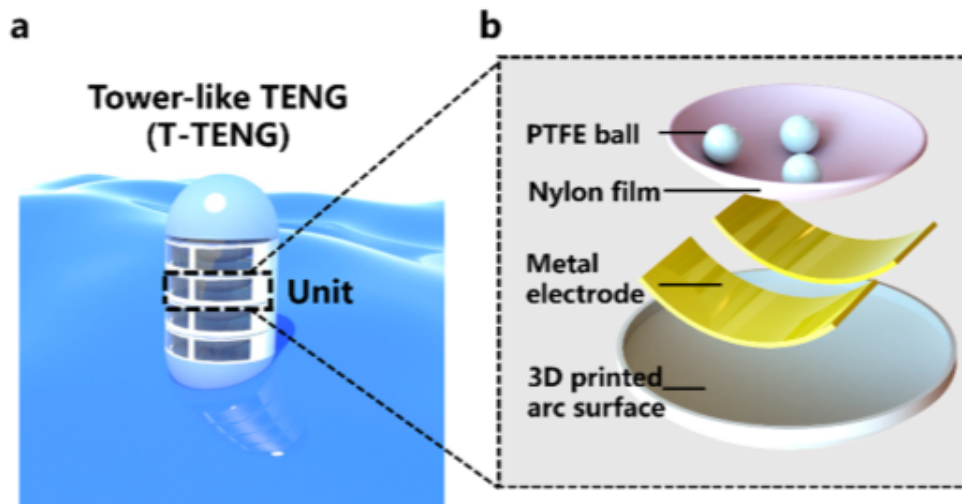
FIGURE 2.16: Tower-like TENG (T-TENG). (a) Complete structure deployed with multiple units inside. (b) Internal structure of one individual unit of the T-TENG [32].

The second prototype (Figure 2.17), called sea snake TENG (SS-TENG), has several units organized in columns and layers, where each one of these units has balls moving around with the movement of the waves. The SS-TENG used in the study had six columns and five layers, totalling thirty units per device. These had a maximum power density of 3.5 W/m^3, calculated with four SS-TENG in a sea-snake network configuration [33].

The next prototype, called soft-contact model spherical TENG, uses a moving object to generate energy with ocean waves as the example showed in Figure 2.18 (a). This object
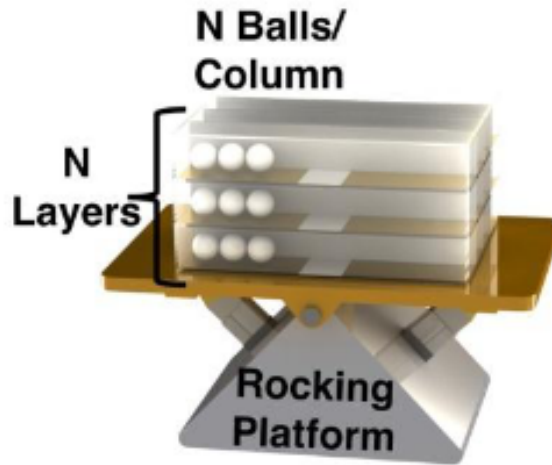
FIGURE 2.17: SS-TENG in a rocking platform used in laboratory tests [33].

is a liquid-filled silicon rubber ball, that generates energy when the prototype rolls. The silicon rubber used shows better results than using the usual PTFE, achieving a maximum power output of 10 mW, 8 times higher than using PTFE [34]. In Figure 2.18 (b) it can be observed that this prototype can generate enough energy to turn on a large quantity of LEDs.
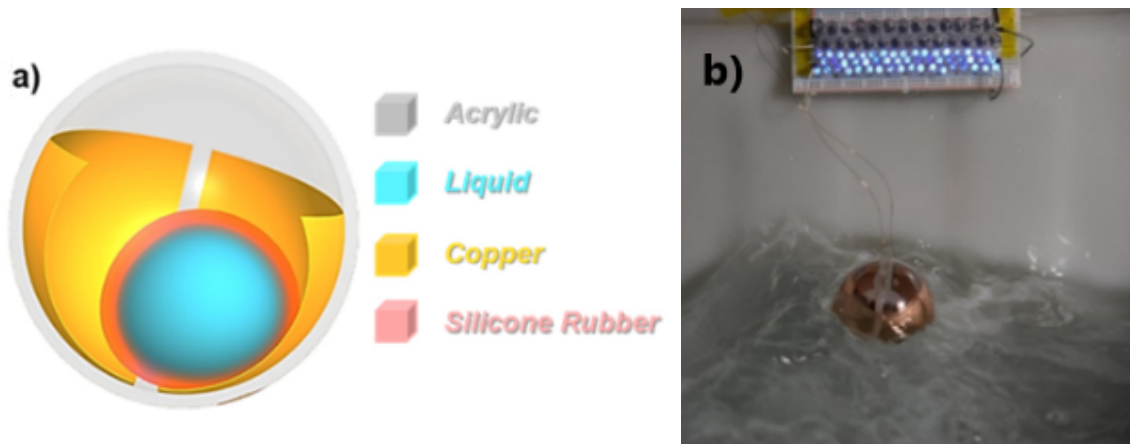
FIGURE 2.18: (a) Schematic of the soft-contact model spherical TENG and (b) Demonstration of this prototype as a power source to light a group of LEDs [34].

The bouy showed in Figure 2.19 (b), has 6 TENGs inside its structure, generating energy with these multilayered TENGs. This type of TENG have copper and FEP films as triboelectric layers and a mass between sponges working as a counter weight to generate more movement for energy generation. Units like those of Figure 2.19 (a) are then stacked into a bouy. This group of 6 TENGs, can generate an average output power density of 13.2 mW/m^2 with a frequency of motion of 2 Hz and it is capable of supplying energy

to an autonomous low power wireless communication system for ocean environmental
monitoring.
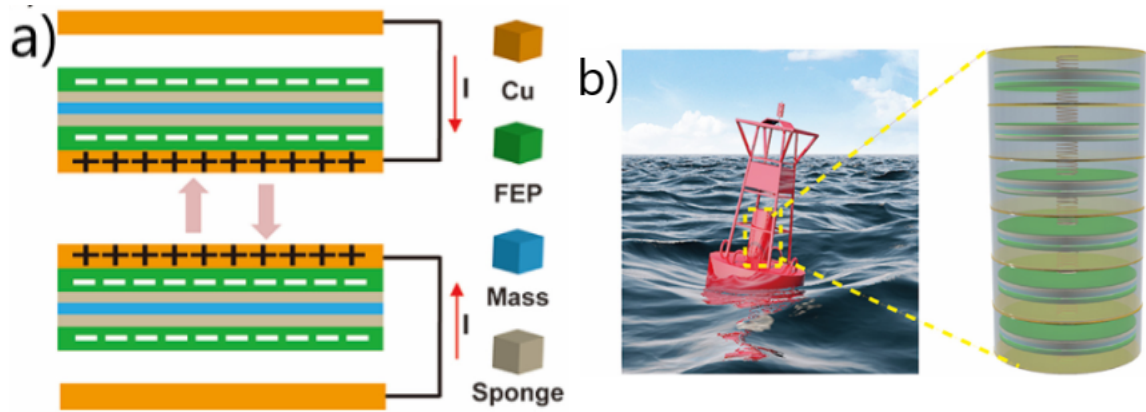
FIGURE 2.19: (a) Working mechanism of the contact-mode TENG and (b) Structure of
the designed multilayered TENG in buoy [35].

The next prototype shown in Figure 2.20 (a), displays a duck-shaped TENG with Ny-
lon balls rolling above a kapton surface. Under that surface there is an electrode to con-
duct charges between the freestanding electrode surfaces. The duck-shaped structure was
built to efficiently harvest energy with the motion of ocean waves, achieving outputs with
3 units of 1.366 W/m^2 [36].

Finally, one last prototype is showed Figure 2.20 (b). This prototype is very similar to
the previous discussed, having a duck-shaped structure, but now with a hybrid system
combining a TENG and a EMG. The prototype has an optimal theoretical frequency of 2.5
Hz, maximum output power densities of 213 and 144 W/m^3, optimal resistances of 280
MΩ and 1.5 Ω, maximum voltage of 390 V and 180 mV and maximum current of 7.2 μA
0.12 A, for the TENG and EMG respectively [37].
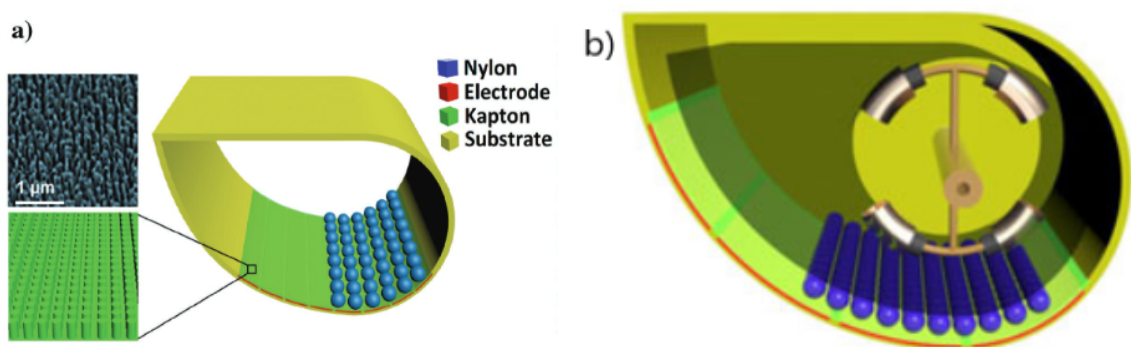
FIGURE 2.20: (a) Structure of the duck-shaped TENG [36] and (b) Structure of the duck-
shaped TENG-EMG [37].

Chapter 3

Development of acquisition and processing methods for triboelectric nanogenerators

This chapter will present the systems developed during this dissertation for both triboelectric nanogenerators data acquisition and processing. These tasks can be extremely time consuming and we therefore developed automated methods for the full characterization of triboeletric devices. First, we will explain how the experimental setup works and the type of devices we used to test and validate this system. These tests were done in order to understand the dependency of the output power of different triboelectric devices on the load resistance, amplitude and period of the motion. The developed setup tries to simulate ocean waves and for that, we need long periods of acquisition time and consequently have large amounts of data to process. Thus, the second method developed was a computational tool used to automate the data processing for each triboelectric device which will be explained in detail, with the help of figures and a work-flow diagram.

3.1 One rotation direction test structure

In the mechanical system developed for data acquisition and testing of triboeletric devices, we will first describe the corresponding structure. This structure only rotates in one direction, enabling the possibility to study some generic proprieties of ocean wave motions, like pitch and roll. This makes this structure optimal to study independently, for

example, the dependency of the power output of each triboeletric device on pitch and roll
motions.
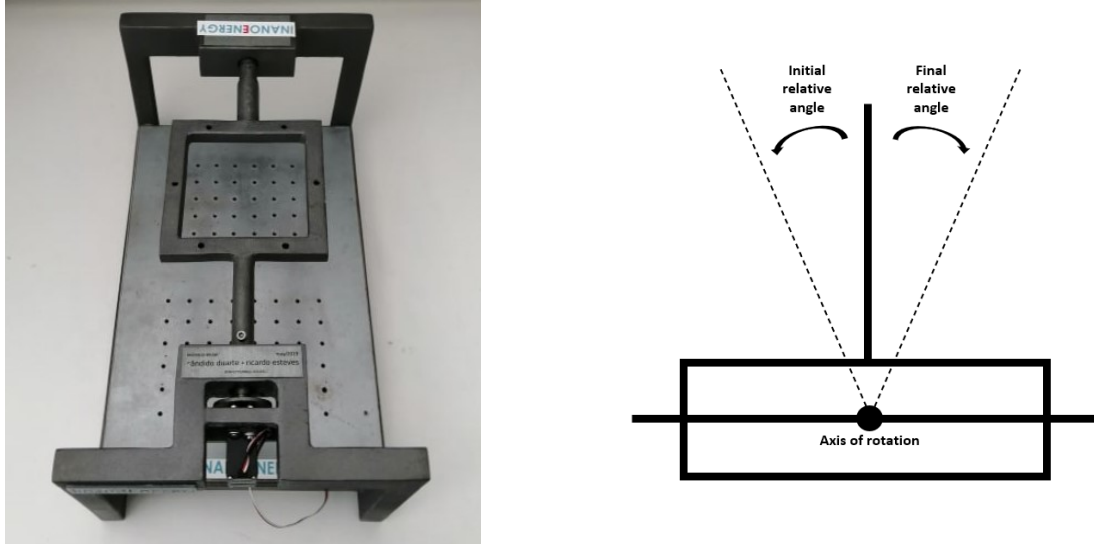
FIGURE 3.1: Top view of the test structure without a device on top.(a) Top view of the
ISOTENG prototype and (b) Lateral view illustration of the ISOTENG prototype.

This mechanical system is made with the combination of a small metal structure and
a servomotor attached on the axis of rotation (Figure 3.1). The servomotor will be con-
trolled with an Arduino Uno. This microcontroller will be able to realize angles of 180º,
90º for each side with small steps of one degree. Regarding the period of rotation, it will
be able to make rotations with a minimum period of 500 milliseconds. In this dissertation
the interval of angles used for each side will be between 8º and 26º with a total rotation
between 16º and 52º, and the interval of periods between 1486 and 7071 milliseconds.
This two intervals will be important on the study of the dependency of the amplitude and
period on the output of TENGs. In appendix A is listed the basic code to upload into the
Arduino Uno, making it control the servomotor, which will only have three input vari-
ables to change throughout every test made with this structure. These three inputs are the
Initial and *Final* relative angles of the servo (in degrees), and the *Period* (in milliseconds),
defining the period of rotation. With only these three input variables, we see how easy it
is to change the amplitude and the period of rotation for each test we wish to do.

The acquisition of data from the devices is made with Keithley High Resistance/Low
Current Electrometer 6514. This electrometer has a huge input impedance (>200 TΩ),
meaning that it has the capability to measure voltage with huge resistance in parallel,
without losing precision of measurement. This is aided by the guard mode this device
possesses, enabling the electrometer to measure voltages with a parallel resistance of 200

GΩ. The guard mode is an important component of the electrometer. For example, in circuits with a higher capacitance than expected, if you have a cable with capacitance of 10 pF and a resistance in the measuring circuit of 50 GΩ (knowing that your time constant is τ = RC), this results on a τ = 0.5 s, making the time for a precise reading of about 2.5 s, ruining the results from the specific device measured. After this, we know that the electrometer, with guard mode on, can measure voltages up to $\pm$200 V, with a source resistance of 200 GΩ and an error under 0.1% [38]. The current that this electrometer can measure is up to 20 mA. A last detail, that can impact in the acquisition of data, is the area each device possesses, which can impact in the increase of the respective capacity. This is why the usage of guard mode is so important, besides the multiple leakage currents that can follow, which could degrade the precision of measurement this is avoided by proper shielding of the guarding structure, with Kelvin clips of cable connection and with the force/sense circuitry approach used by the electrometer.
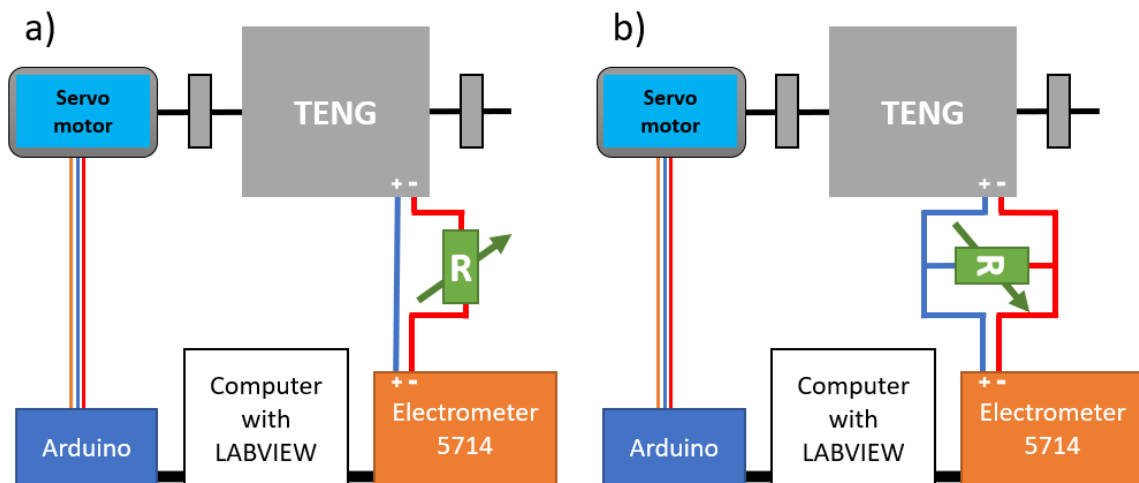
FIGURE 3.2: Acquisition setup for TENGs. (a) Current measurement and (b) Voltage measurement.

The electrometer will be controlled with a custom program developed with Labview, having only to select the destination of the data, selecting between a current or voltage acquisition and their respective ranges. For the change in load resistance in this system, it will be utilized a variable resistance board, controlled by another Labview program, with the only input being the selection of the resistance we want to use. This variable resistance will be very handy when we want to do a test with different values of resistance for current or voltage. All the parts talked in this section can be seen together in Figure 3.2, where two sub figures show the small difference between current and voltage measurements regarding the position of the variable resistance board.

3.2 Triboeletric prototypes used

In each of the TENG prototypes used in this dissertation, the way power is generated is similar. This is done with two opposite triboelectric materials in a form of thin sheets, PTFE with 0.05 millimeters thickness and Nylon 6.6 with 0.017 millimeters thickness, each one of them with a thin layer of silver applied with screen printing techniques. This layer of silver acts as the conducting material in both materials. Also, in every prototype we will have small SS316L (stainless steel) balls making the sheets of PTFE and Nylon cyclically touching, generating power with this motion.

3.2.1 Isotropic floor TENG - ISOTENG

The first prototype called ISOTENG, was tested on a circular structure created with the help of a 3D printing machine, seen in Figure 3.3 (a). It has a diameter of 21.5 cm with a curvature radius of 25 cm. Inside the structure, there are ten stainless steel balls moving, making the opposite sheets of PTFE and Nylon connect and disconnect with the motion of the balls. Also, a net is placed above the prototype in order to disable the possibility of having balls escaping from the prototype.
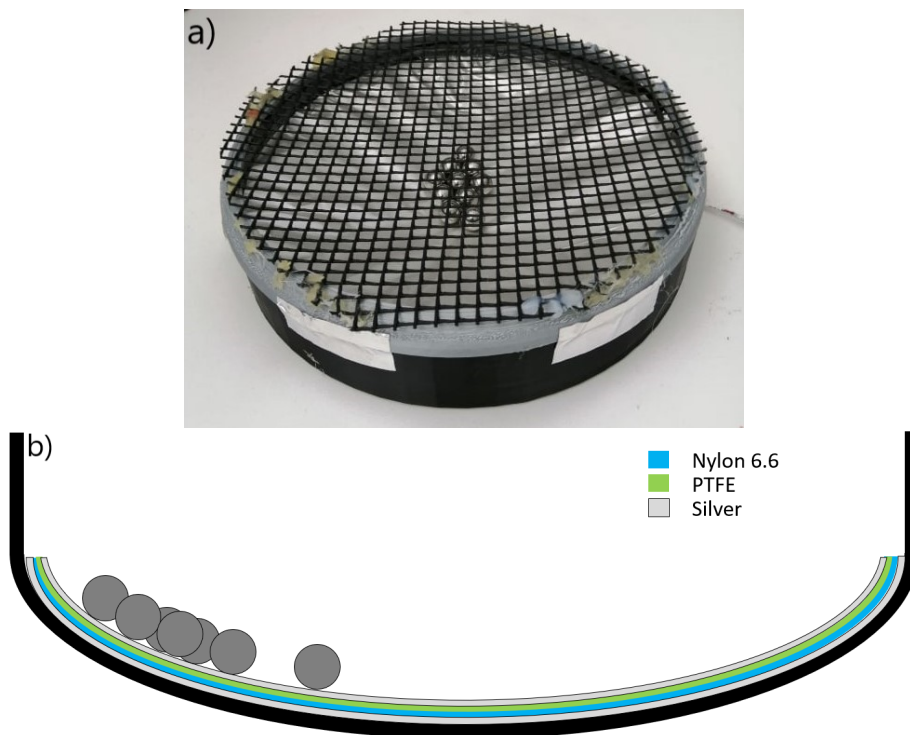
FIGURE 3.3: (a) Top view of the ISOTENG prototype and (b) Lateral view illustration of the ISOTENG prototype.

As can be observed in Figure 3.3 (b), this structure uses the movements of ten balls, to connect and disconnect the opposite sheets on the floor of the device. The colour we see on the bottom of the device is the layer of silver placed on the top of PTFE, which is on the top of a Nylon sheet with silver on the bottom.

Another aspect we can obviously take from Figure 3.3, is that the power output of this device should depend equally on pitch and roll, because this motion should create the same behaviour on the circular device.

3.2.2 Anisotropic floor TENG - ANISOTENG

The second prototype is part of a second structure with multiple tracks, each track being 21.5 cm long. Although it only has two different types of tracks, both use the same type of materials stated before, PTFE, Nylon 6.6 and silver for conducting electrode. Another common thing these two type of tracks have, is that each track was tested using only two stainless steel balls. The structure used can be seen in Figure 3.3 (a).

The second prototype, called ANISOTENG, uses the same dynamic as the first one, having the two opposite materials on the top of each other with the silver layer conducting in between them. The balls moving from one side to the other will make the two surfaces cyclically touch, generating energy as seen in Figure 3.3 (b). The surface of each track has a 4 cm width and 21.5 cm length, achieving a total area for this prototype of 86 cm^2.
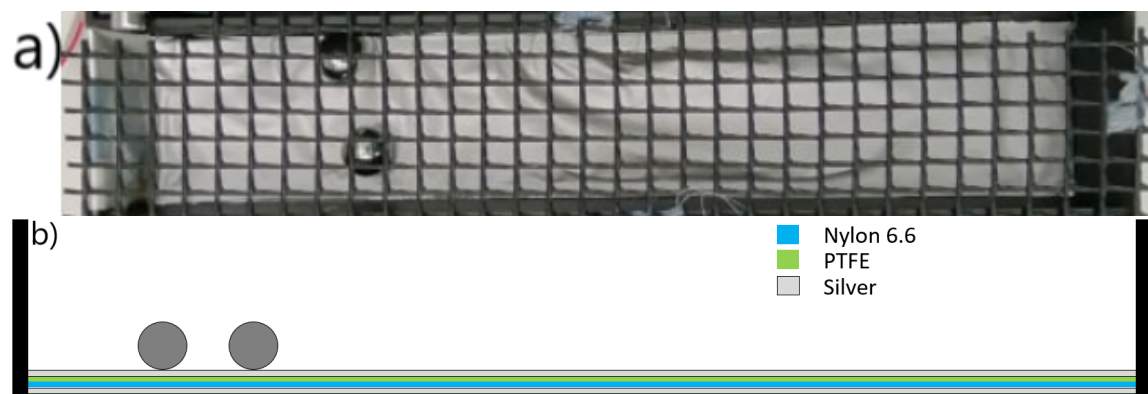
FIGURE 3.4: (a) Top view of the ANISOTENG prototype and (b) Lateral view illustration of the ANISOTENG prototype.

3.2.3 Lateral TENG - LATENG

The third prototype is placed on the lateral walls seen on the structure of Figure 3.3 (a) and is thus, called lateral TENG. This prototype uses the same materials as stated before, but

it only generates power when the balls hit the lateral walls making them achieve contact in between the inside walls of this prototype, seen in Figure 3.5. The inside walls, where the contact happens, have a width of 3.7 cm and a height of 2.6 cm, achieving a total area of 9.62 cm^2.
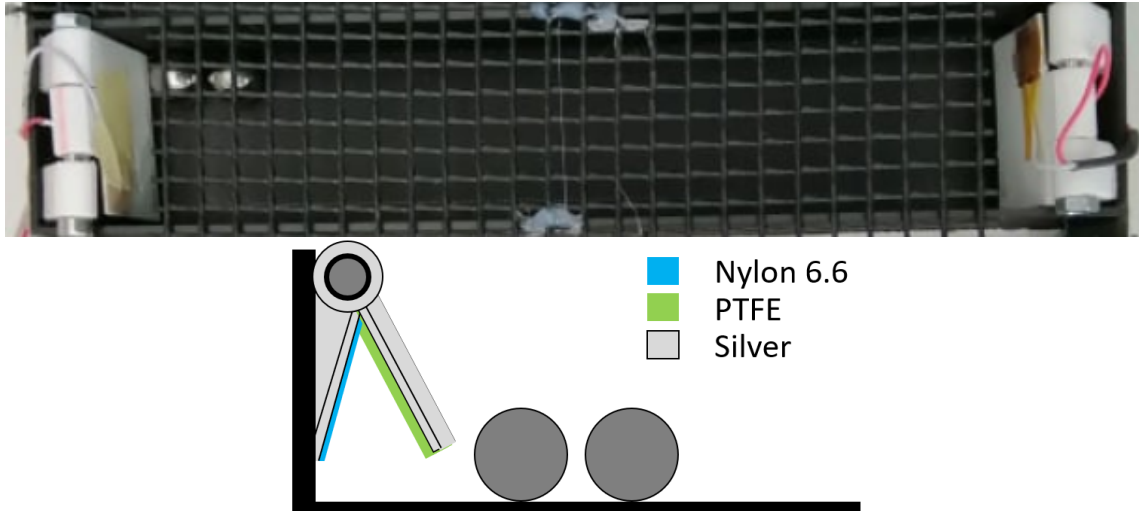
FIGURE 3.5: (a) Top view of two LATENG prototypes and (b) Lateral view illustration of the LATENG prototype.

3.3 Processing software - Development of a computational tool to automatically process data from triboelectric devices

After every data acquisition generated with the setup explained in the last sections, there was always a need to process the huge amount of data it generates. A good way to understand this is, for example, if we want to plot the maximum voltage from a device, for different resistances, we need to manually look for the maximum data point on a plot. If this acquisition takes five minutes it will have about 3 x 10^5 data points ($\sim$1 per ms), this can be very time consuming to do manually. Obviously this is done with software prepared for this type of tasks. Nowadays, if you want to know the maximum point of a large array of data points, you should use a software like M. Excel or even programming languages like Python, making this task automated and easy. The problem in the example stated, is that, when you want to do it for every resistance and then plot the relation of Voltage with different values of Resistance, you should do this with one of the options stated above.

After that, we arrive to the main problem with TENGs data processing, which is to acquire an average value for the local maximum data points, which in these experiments should be periodic, done by the motion of the balls in each prototype. This average value, will give us a better notion of the actual output each device will have in each circumstance, being the change in resistance, amplitude or period of the motion. For this, we will use Python as a tool to help us achieve automation on this data processing, which normally would take large amounts of time to process, and now it is done within a few clicks.

3.3.1   Algorithm development to detect an average for local periodic maximums

In TENG devices, one of the most important characteristics to know, is their optimal resistance, and with this we will know how to generate their maximum power output. The usual ways to show this dependency on resistance is to use the maximum voltage and current for each resistance. Then, multiplying these values, we achieve the power value dependent on resistance, showing the typical peak at a given load resistance value and then decreasing the power output when you increase or decrease the resistance value. As it was stated before, in some cases this is not the best way to understand the way each device outputs energy. Another way to visualize how TENG characteristics change with, for example, the resistance, is to look for an average value of the local maximum points. This is done because, when testing with different resistances, you obviously should do the same motion in each experiment with a different resistance. This type of motions should be periodic, making the appearance of local maximums per period almost a certain event.
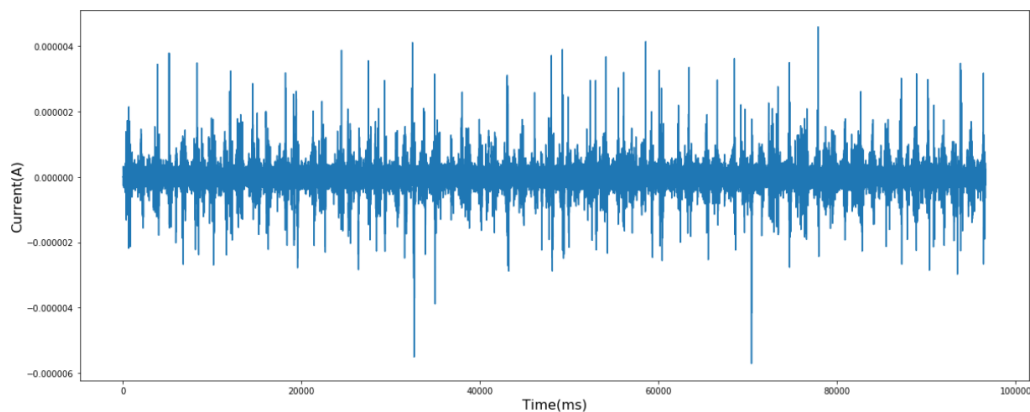
FIGURE 3.6: Raw data example of a current measurement with a resistance of 100 kΩ on the ANISOTENG prototype.

In Figure 3.6, we can see a raw example of a measurement of current for the ANISOTENG prototype, having about 100 seconds of measuring time with a resistance of 100 kΩ. The

plot shows easily identifiable periodic local maximum points. These are the ones we want to calculate the average value and then compare them with the values of, for example, different load resistances. After this step, the same should be done with the voltage, and with it, we can acquire the power value and plot these three units in the same plot, to compare them and observe their behaviour.

The way the developed tool works is by using four main processes that will be described extensively on the next sections. In Figure 3.7, we can see the flowchart diagram, which describes the workflow of the software tool.
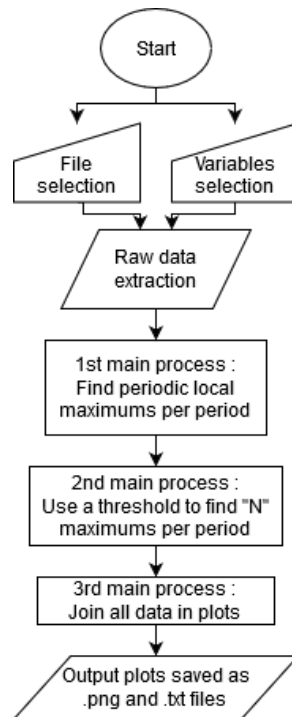
FIGURE 3.7: Flowchart of the software tool.

3.3.1.1   1st main process - Find the average value of the maximum local data points per period

The first main process is to go on each period and look for maximums or minimums data points. This division is made because, as said before, we suppose that the signal should have at least N maximum or minimum points per period, made by the different motions. This N value (an integer) depends on the setup we are using. For example, on the ANISOTENG prototype, the balls will create two large spikes, due to the motion of the balls going from one side to the opposite, twice per period. With this knowledge, we should ask the algorithm to search for two maximum and minimum per period, on

this prototype. This search will not be the simple search for two maximums per period, because we can have two spikes together in a very small time period, which will not translate well for the real average value of the spikes. For this, we divide the period in two and search for a maximum in each half period.
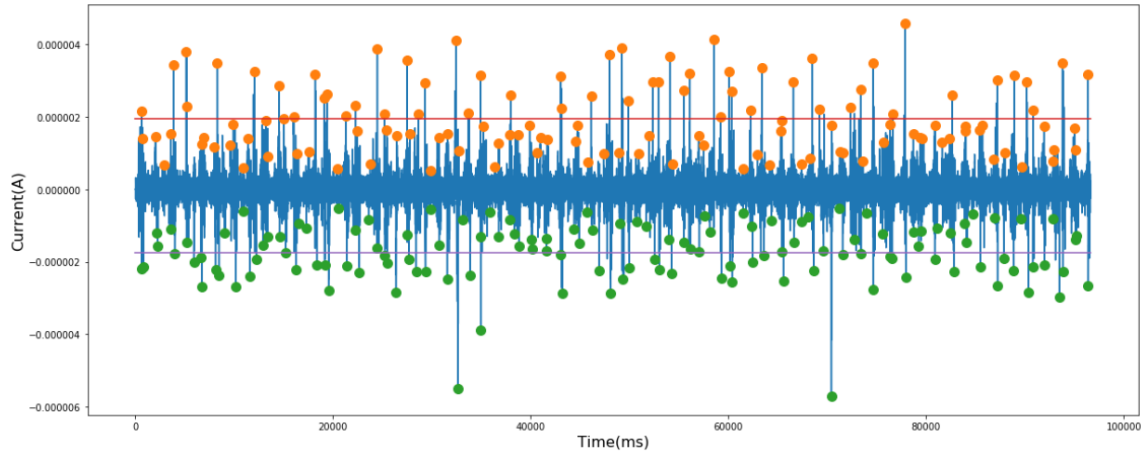
FIGURE 3.8: Detection of N maximum and minimum points per period and their averages.

This step of the algorithm is shown in Figure 3.8. We can see, as orange dots, the points acquired as maximums in each period, and, as green dots, the points acquired as minimums and on each side, a line to enables us to visualize the value of the average made with all of those maximums and minimums.

As we can see from Figure 3.8, the acquired data points are not always the expected true maximums and minimums. With these data points we can go into the next step, to acquired only "real" maximums and minimums per period as requested.

3.3.1.2 2nd main process - Using a threshold value to find N maximum data points per period

The second main process happening within the algorithm is where things get interesting. It was observed before, that the search for two maximums and minimums, in each of the two sub periods, does not bring results as perfect as we wish them to be, having some points that are obviously out of the zone we want them to be picked out from.

Next, with the points picked out from the last process, there is an average value and also a distribution, that we can approximate to a normal distribution. This approximation is easily made with the help of Python libraries like Scipy, particularly the scipy.stats.norm

function, which enables us to approximate a collection of data points to a normal distribution function, having as outputs the average and standard deviation values of that distribution. This enables us to subtract the standard deviation multiplying by a portion called *Beta* (another input of the algorithm), in the case of the positive fraction, maximum's distribution. In the negative fraction, *Beta* is multiplied by the standard deviation and then we sum to the average of the minimum's distribution. These two new values, are then used to create a sort of threshold, which is used to determinate a boundary from where the algorithm starts looking for maximums or minimums. The value of the input *Beta*, with a recommended value of 1, is not a perfect value for every acquisition, but it has close to perfect results in every device.

The amount of maximums or minimums, that the algorithm looks for is determined by an input in the beginning called *N*. This input has to be an integer, with typical values like 1 or 2 in this dissertation.

Figure 3.9 shows the results from this process, where in this case, it is observed that there are no points acquired too low in the signal. Also, the points which are acquired are always local maximums or minimums, because we acquire only *N* maximums or minimums per period and there are no excess data points acquired.
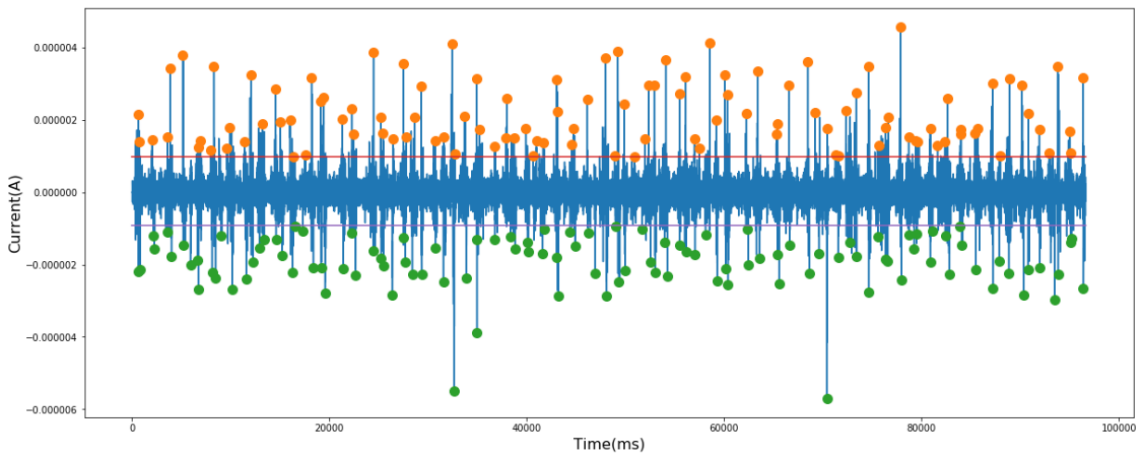
FIGURE 3.9: Detection of local maximums/minimums above/under a certain threshold.

In the case of Figure 3.9, the only data that the algorithm saves from each acquisition, after passing into these two steps, is the average value of the local maximums and minimums. The saved data is then used in the plotting phase of the algorithm, which will be explained below.

3.3.1.3   3rd main process - Joining all of the processed data from a TENG device into plots

After the data, from a particular device, has been processed, the results need to be visualized and compared. For example, if the study is the behaviour of voltage and current with the change of resistance, the plot should show both values in a different y-axis, having in the x-axis the resistances tested.
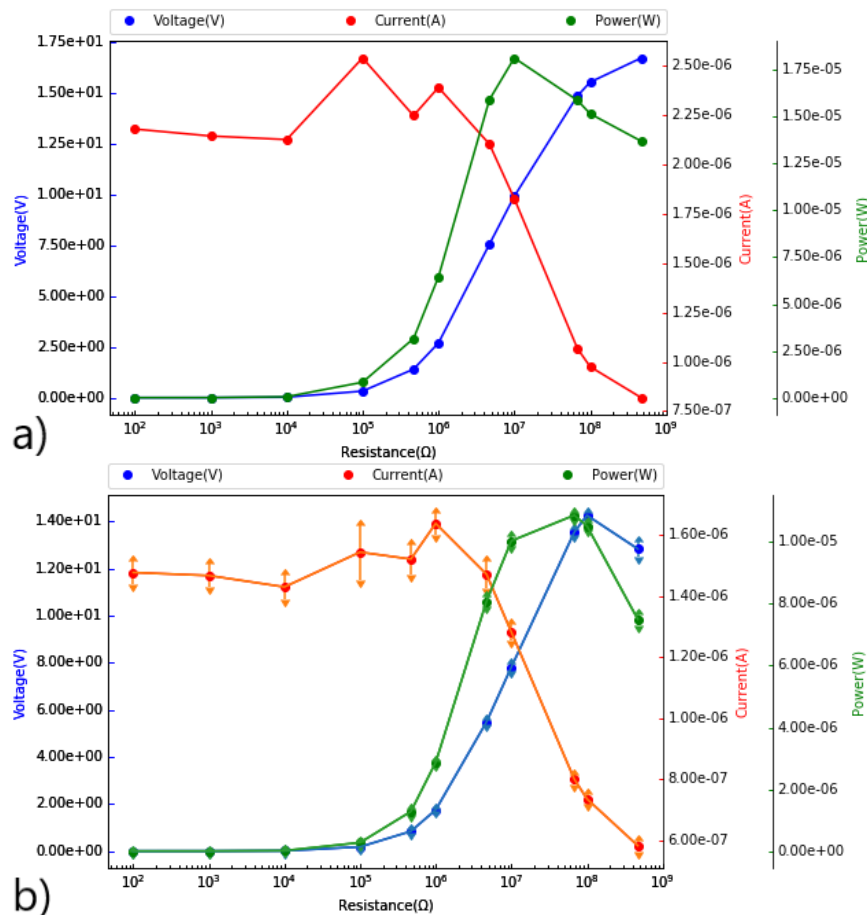
FIGURE 3.10: (a) Maximum values for each measured quantity and (b) Average value of the local maximums for each measured quantity with a standard deviation as error bar.

After this, another thing to visualize and understand is the respective power that each device generates with every resistance tested. As stated before, this is done by multiplying voltage and current, having now three y-axis to be compared in the same plot. This plot will have two type of points, which are just maximum values for each resistance (Figure 3.10 (a)) or the average value of local periodic maximums (Figure 3.10 (b)). This second type of plot will show error bars, representing a standard deviation of the distribution of points used for that average. Because the power data points are derived from the voltage

and current values and we need to calculate the standard deviation of the power values, this is done by error propagation, which in this case will be done with the most simple method:

$$\sigma_P = \sqrt{\left(\frac{\partial P}{\partial V}\right)^2 \sigma_V^2 + \left(\frac{\partial P}{\partial I}\right)^2 \sigma_I^2} = \sqrt{I^2 \cdot \sigma_V^2 + V^2 \cdot \sigma_I^2}. \tag{3.1}$$

From this point on, these two types of plots will be used to compare voltage, current and power of a particular TENG device with, for example, the variation of resistance, period or amplitude of the device's motion. These two types of plots can be observed in Figure 3.10.

3.3.2 Comparing with an older and more time consuming method

A good way to understand how this software tool behaves is by comparing it with another method of data processing. This alternative method is done with the help of OriginLab software, having a semi-automatic nature as, for each graph as the one presented in Figure 3.6, we need to input a positive or negative threshold, to find positive or negative local maximums, having to do this repeatedly and resulting in a highly time consuming method.

In Figure 3.11 we can observe the results from the 2 different methods. The plot from the computation tool does not have the power values for a better visualization of the voltage and current. These results, coming from a test device that has a very good periodic motion and output, show small standard deviations, making this data set the best for analysing how good the methods are.
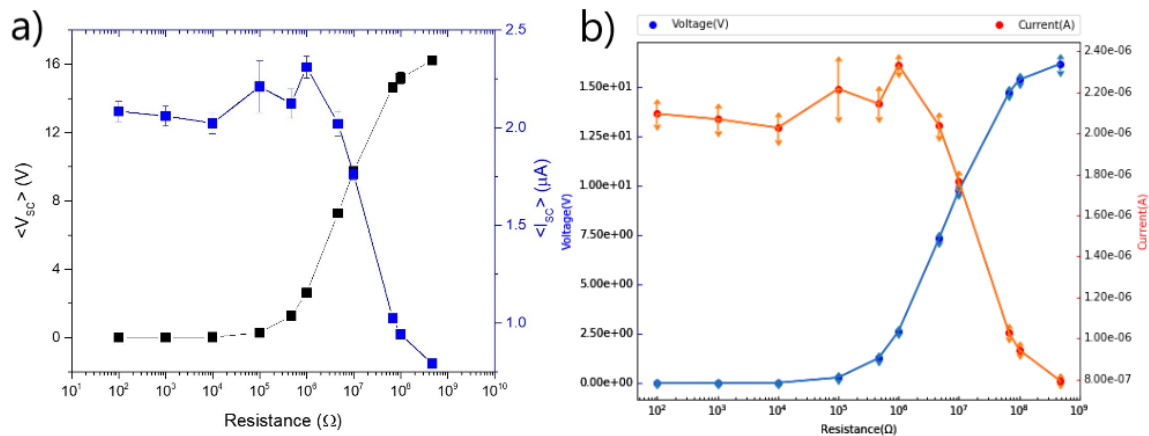
FIGURE 3.11: (a) Results acquired with an acquisition method which uses semi-automatic processing and (b) Results acquired with the computation toll which uses automatic processing and was developed in this dissertation.

The similarities between both methods are very obvious, almost having exactly the same results and standard deviations, showing how good the new toll is on processing and analysing data from TENGs, compared with the more time consuming method.

3.3.3 Output dependency on the Period and Amplitude of the motion

Another interesting study on a TENG device, is how the output quantities, like voltage, current or even power, depend on the period and amplitude of the motion made by the TENG. This type of tests will need a new Arduino Uno code, as showed in Appendix B, in order to control the servomotor, because, to automate this series of tests, the amplitude and period needs to be changed on each test. This is done by sending a message by Serial communication with a USB cable and some modifications on the original Labview program, making this tests automated and easy to do. The results will look like Figure 3.12, showing the dependency of the open circuit voltage on the amplitude and period of the motion.
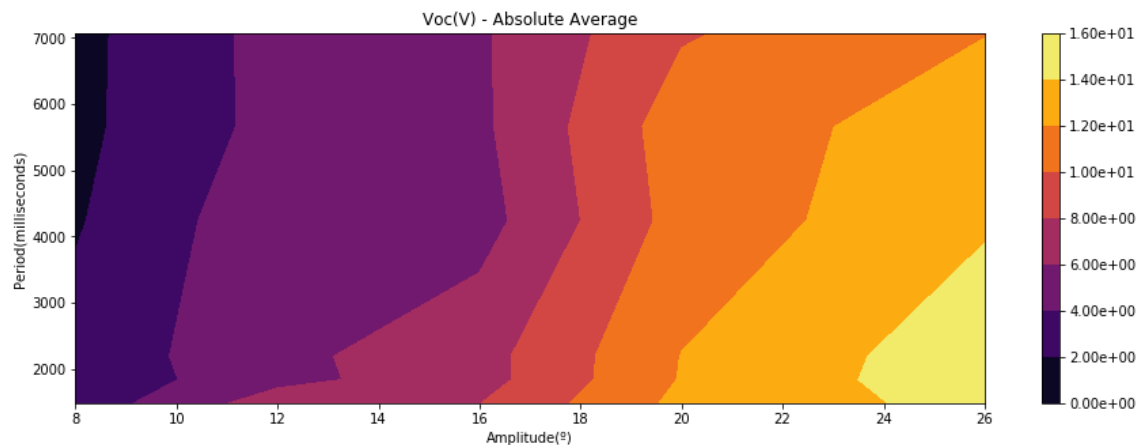
FIGURE 3.12: Average of the local positive maximums for combinations of amplitude and period for a measured quantity.

Chapter 4

Blue energy harvesting - TENG's characterisation

In this chapter we present the results obtained with the experimental setup and software tool created to analyse and process the data acquired from TENGs. In each section, a specific type of TENG will be studied, having a resistive load characterisation for that specific TENG and a study on the dependency of the output of the TENG, with the period and amplitude of the induced motion (pitch rotation). A common factor with all studied TENGs is that the yaw direction of rotation will have a very small and negligible importance on their output values. Because multiple TENGs will be experimentally studied, at the end of this chapter, a general comparison of the most important values will be discussed.

4.1   Isotropic floor TENG - ISOTENG

The first TENG to be studied is the Isotropic floor TENG (ISOTENG). ISOTENG is isotropic because it has no directional preference for movements done on the pitch and roll rotation directions. This is possible because the circular structure can be seen has multiple direction strips and obviously, when ocean waves move the ISOTENG in isolated pitch and roll directions, the output should be the same. Also, when ISOTENG is moved in combined rotations in pitch and roll directions, their combination should give better results than a simple rotation in pitch or roll directions. These will be the distinctive factors to differentiate this TENG from the other showed in this work.

The mechanism of the ISOTENG will be the same as that of the ANISOTENG. These two prototypes use the same type of operating mode to generate energy, the only differences will be the curvature of the surface of the prototypes, the number of balls used and the freedom that the balls have to go around each prototype. This is the reason why the explanation for both of these prototypes will be given in the ANISOTENG subsection.

4.1.1   Resistive load characterisation

The first and most important analysis to do on a TENG is the resistive load characterisation. This was done by putting the TENG subject to the same motion for each measured quantity and different resistances used, and verify what resistance optimized the power output of the TENG. This motion had a period of 1486 milliseconds and an amplitude of 26º, which were the minimum and maximum values used in this work respectively. The testing time per resistance/period/amplitude was 100 seconds. In Figures 4.1 (a) and (b), the output voltage with that motion and a resistance of 470 kΩ is showed.

The ISOTENG has the expected output tendencies. The voltage increases and converges to a maximum value ($\sim$15 V) with the increase of the resistance, while the current has the opposite behaviour, converging to zero coming from a maximum value ($\sim$2.25 μA) reached with low resistances. Finally, the power will have a maximum value ($\sim$6.5 μW) reached on its optimal resistance and converges to zero if the resistance increases or decreases from this optimal resistance value (10 MΩ).
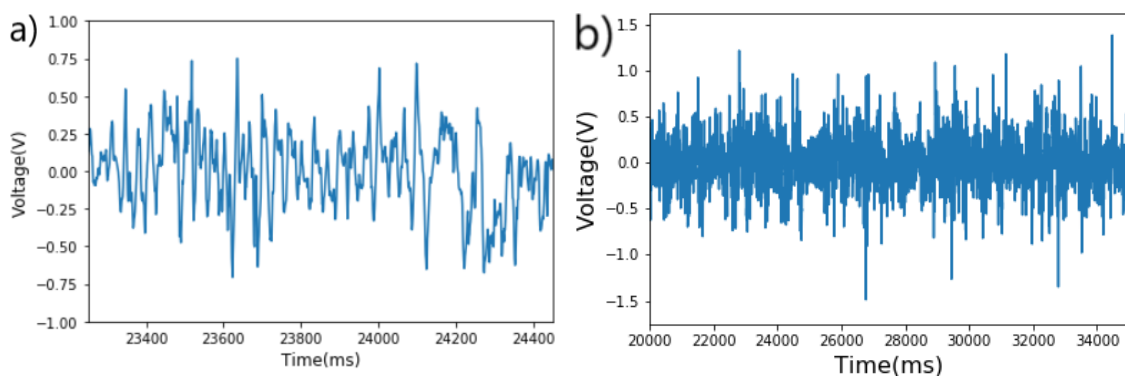
FIGURE 4.1:   Raw data output of voltage with a resistance of 470 kΩ. (a) One period of motion of the ISOTENG and (b) Multiple periods of motion of the ISOTENG.

The results showed in Figures 4.2 (b) and (c) show a clear similarity between the negative and positive averages of local maximum points, having a symmetrical behaviour, showed in Figure 4.1. This will result on a absolute average as showed in Figure 4.2 (a), being very close to both negative and positive averages in the case of the ISOTENG. The

results show that, for the group of resistances used, the one where the power output is maximum was the 10 MΩ resistance, with a 7.83 μW average absolute power output.

FIGURE 4.2:   Average value of the local maximums for each measured quantity with a standard deviation as error bar, having the colours blue, red and green for the voltage, current and power respectively. (a) Absolute average value. (b) Negative average value. (c) Positive average value.

4.1.2   Output dependency on the Period and Amplitude of the motion

In this section, it is discussed how the output behaves with different values for the period and amplitude of the motion made by a TENG. In the case of the ISOTENG, we see clear

tendencies to raise its output with the increasement of amplitude and decreasement of period (Figure 4.3).

Although all the tendencies are as expected, the power output, at the optimal resistance is lower by 90% than the values presented in Section 4.1, when it generated 7.83 μW for a 26º amplitude and 1476 ms period of motion. In this study, with the same amplitude and period, it generated 0.69 μW. Because these two studies were made at a time interval from each other, the conclusion is that some sort of degradation occurred in this specific TENG. This is why in the next chapter this degradation hypothesis will be studied.

Also, we see an almost perfect tendency on the voltage measurements, but when we observe the current we see that some parts seem out of place. This is because the current measurements at these low values of current, as Figure 4.3 (b) shows, have noise that makes the signal not as perfect as the voltage measurements.

FIGURE 4.3:   Results showing the dependency of multiple output quantities with different values of period and amplitude. (a) Absolute average value of V_{OC}. (b) Absolute average value of I_{SC}. (c) Absolute average value of power with the optimal resistance for the ISOTENG.

4.2   Anisotropic floor TENG - ANISOTENG

The second TENG to be studied is the Anisotropic floor TENG (ANISOTENG). ANISOTENG is anisotropic because it has a directional preference for movements done on the pitch and roll rotations directions. This happens because the ANISOTENG has a long stretch where the balls can move and produce energy. When the movement is along the width direction, the production of energy will be too small, compared with the same movement being done in the length direction. This is why the tests were done along the direction of higher energy production. If we tried to study this TENG with combined rotations in pitch and roll directions, the results would be very close or lower than isolated rotations done on the length direction. They could be lower due to the loss of energy when the balls hit the walls, making them slower or incapable of reaching certain positions in specific periods of motion.
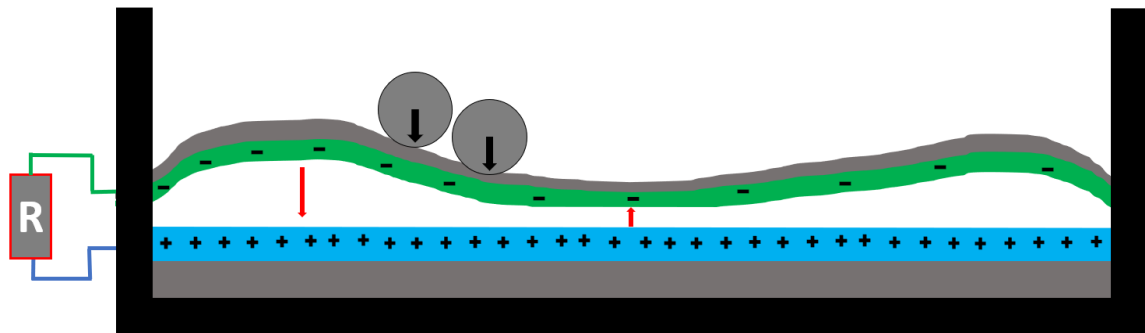
FIGURE 4.4: Schematic of the ANISOTENG prototype motion.

The way this prototype generates energy is illustrated in Figure 4.4. First, the balls will be moving above the two triboelectric surfaces, this will make charges flow from one triboelectric surface to the other. In this case this prototype mechanism of energy generation will not be a simple contact-separation mode TENG, because we have multiple wrinkles with different sizes and when the balls pass above them, they will induce contacts between the surfaces below. This contact should be like a classical TENG contact-separation mode but with multiple wrinkles being squashed at the same moment by the weight of the balls and even more during one period of motion. This will create a type of output much more chaotic than the classical TENG contact-separation mode with only two spikes.

The mechanism explained, will be very close to the ISOTENG mechanism with the only difference between them being the curvature of the surface of the prototypes, the number of balls used and the freedom that the balls have to go around each prototype.

4.2.1 Resistive load characterisation

In Figures 4.5 (a) and (b), the output voltage of the ANISOTENG with the standard motion and a resistance of 470 kΩ is showed.

The results for the ANISOTENG (Figures 4.6 (a), (b) and (c)), do not show the typical behaviour of the power output. This happened because the measurement of the current values was not decaying as it should have been. The reason for this comes from the low output current that this particular TENG has, combined with some noise on the measured signal. The resulting measurement will have a small standard deviation and will not change much with the increase of the load resistance.
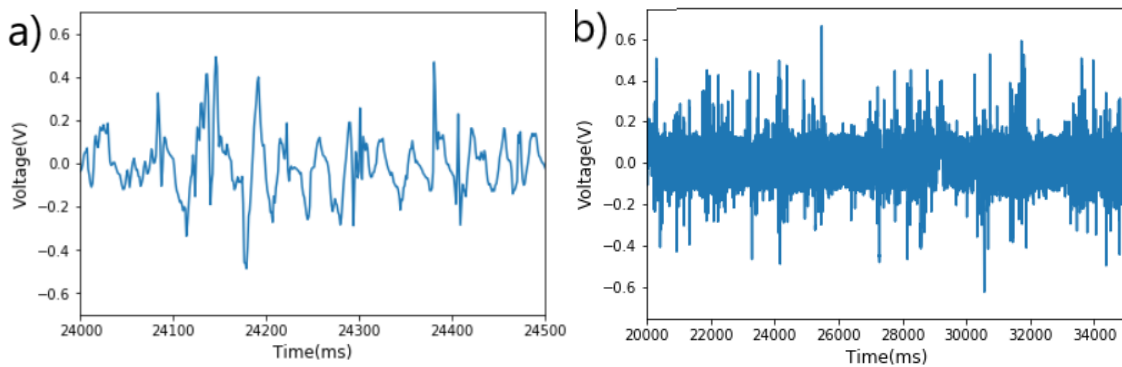
FIGURE 4.5: Raw data output of voltage with a resistance of 470 kΩ. (a) One period of motion of the ANISOTENG and (b) Multiple periods of motion of the ANISOTENG.

The results shown in Figures 4.6 (b) and (c) show a small difference between the negative and positive averages of local maximum points, having an almost symmetrical behaviour, showed in Figures 4.5 (a) and (b), but this does not agree with the results showed. This is because, in the voltage measurements, there are 2 or 3 outliers points that make the value of the positive average, for the higher resistances, increase slightly compared with the negative.

The resulting figures and results point as the optimal load resistance being the highest tested, 470 MΩ, with 4.44 μW average absolute power output. However, as stated above, we know that the measurements on the last 3 resistances should be lower that the presented. With this in mind, the best resistance should be the 10 MΩ for the ANISOTENG.

4.2.2 Output dependency on the Period and Amplitude of the motion

In the case of the ANISOTENG, we see clearly the same tendencies, raising its output with the increase of amplitude and decrease of period of motion, as shown in Figure 4.7.
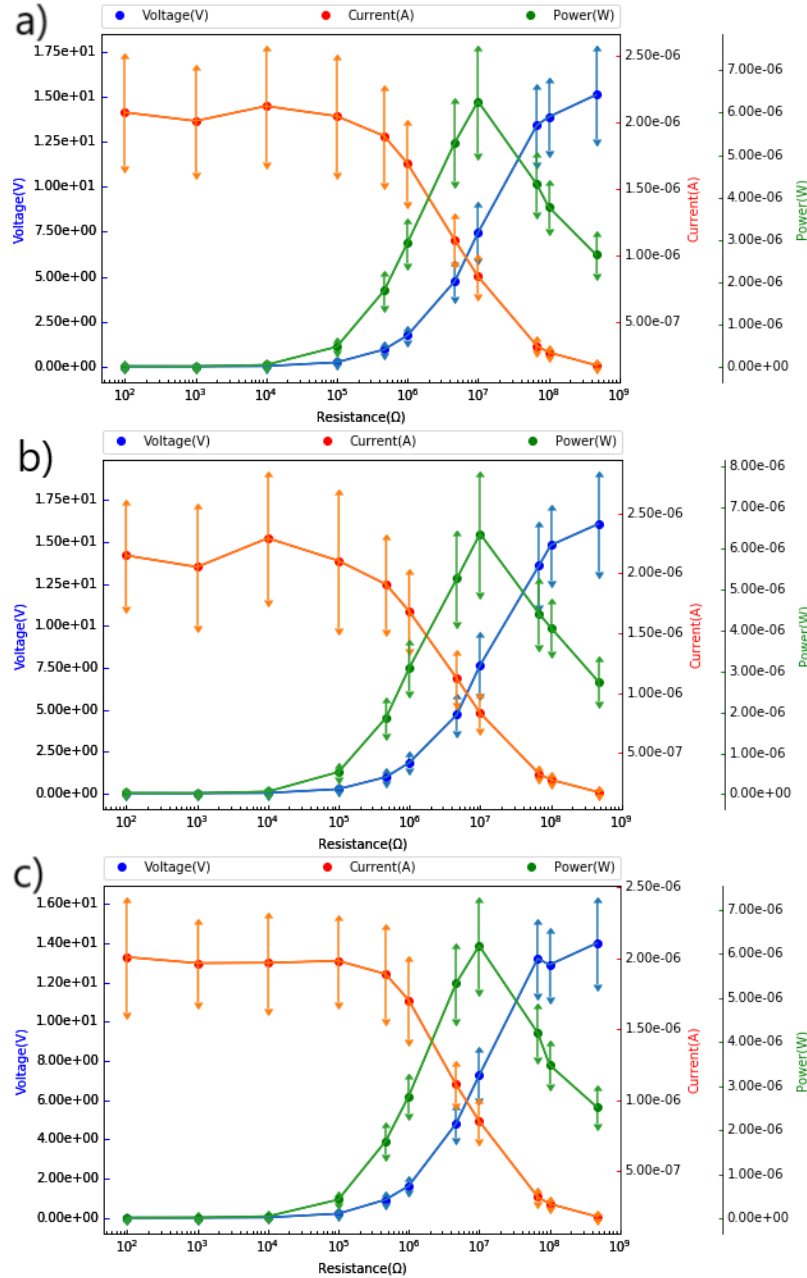
FIGURE 4.6: Average value of the local maximums for each measured quantity with a standard deviation as error bar, having the colours blue, red and green for the voltage, current and power respectively. (a) Absolute average value. (b) Negative average value. (c) Positive average value.

Although all the tendencies are close to the expected ones, the power output, with the optimal resistance, was less than 5% of the expected value. The ANISOTENG was generating 3.28 μW, with the optimal resistance, 26° amplitude and 1476 milliseconds of period. In this study, with the same amplitude and period, it is now generating 0.16 μW.

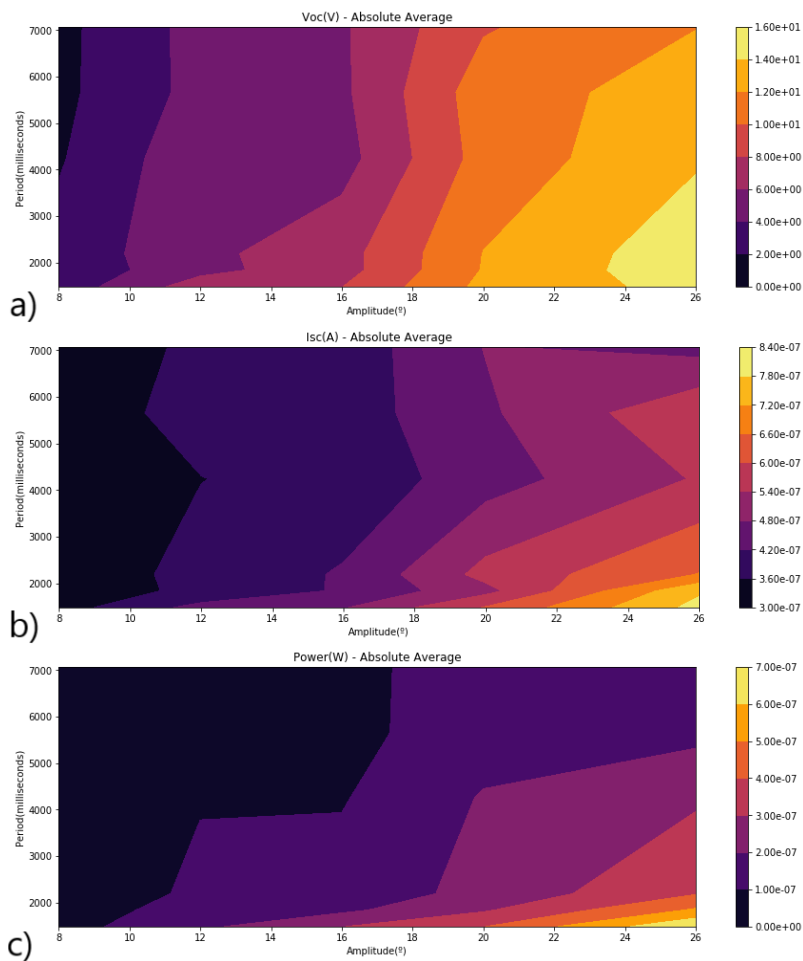We again conclude that some degradation mechanism is also happening to this TENG.
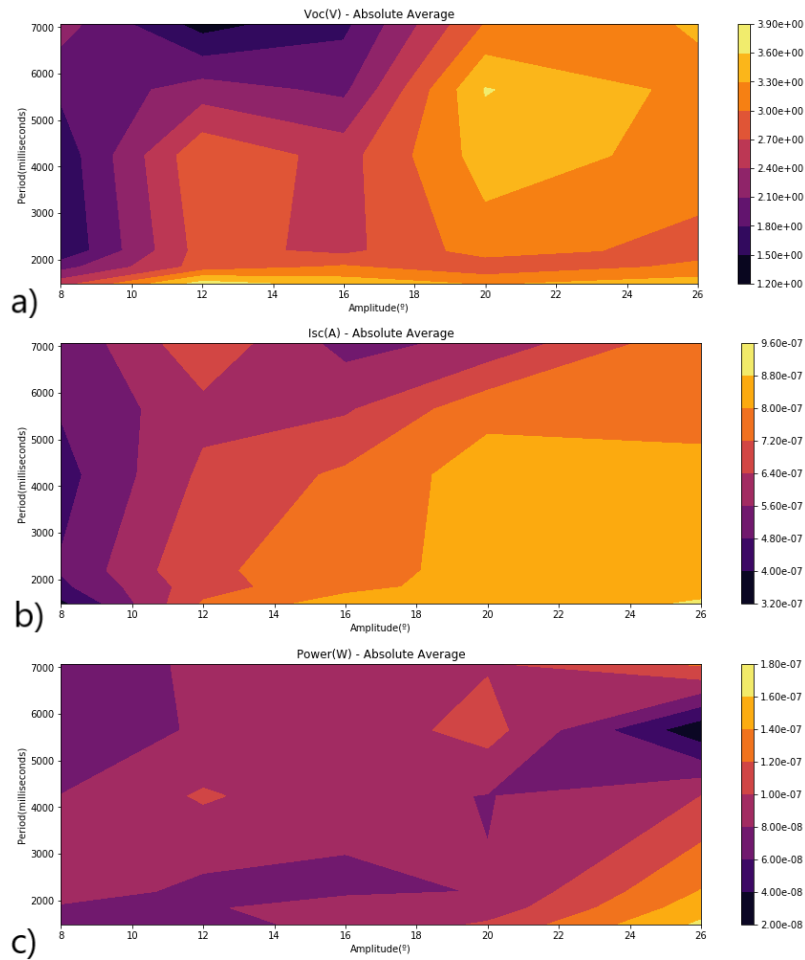
FIGURE 4.7: Results showing the dependency of multiple output quantities with different values of period and amplitude. (a) Absolute average value of V_{OC}. (b) Absolute average value of I_{SC}. (c) Absolute average value of Power with the optimal resistance for the ANISOTENG.

4.3   Lateral TENG - LATENG

Finally, the last TENG to be studied is the Lateral TENG (LATENG). LATENG is very different from the first two TENGs studied, working almost like a classical contact-separation mode TENG, with opposite surfaces coming into contact when the ball reaches and touches the lateral wall. It will be very dependent on rotations along the length direction, because the energy generation will only occur if the balls reach the lateral walls. Combining directions of rotations will not help the energy generation due to that fact, once again, the yaw direction of rotation will have a very small and negligible importance for the output.
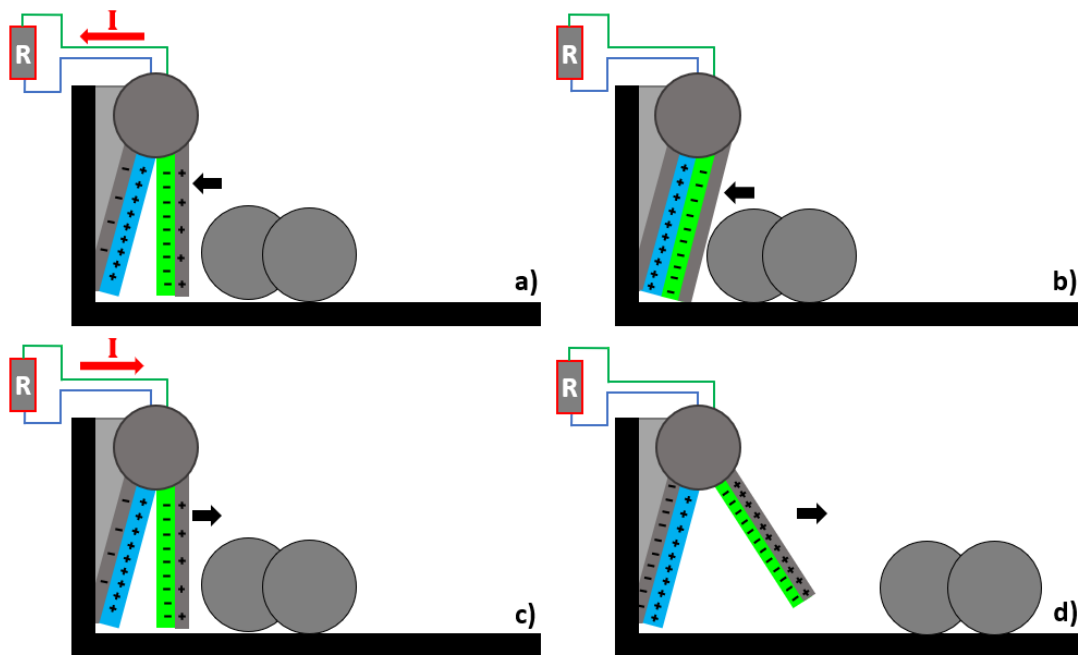
FIGURE 4.8: Schematic of the LATENG prototype motion.

The way this prototype generates energy in one period of motion is illustrated in Figures 4.8 (a), (b), (c) and (d). First, in Figure 4.8 (a), the balls will collide with the moving surface. This will make charges flow from one surface to the other, creating negative and positive charge densities in both electrodes surfaces, and thus a current flow from one electrode to the other. Right after touching, like Figure 4.8 (b) shows, the charges are in equilibrium and will remain like this until the surfaces separate again (Figure 4.8 (c)), when the balls go back to the other side of the structure due to the movement. This will break the equilibrium and make charges flow from one surface to the other creating an opposite current. When the movement of the prototype makes reach the position shown in Figure 4.8 (d) shows, the maximum distance between these surfaces is reached and the charges in the electrodes should be the same for both surfaces.

4.3.1   Resistive load characterisation

In Figures 4.9 (a) and (b), the output voltage of the ANISOTENG with the standard motion and a resistance of 470 kΩ is showed. It has a similar behaviour like the classic contact-separation mode, as expected. In Figure 4.10 (a), we see that the LATENG has the expected output tendencies. The voltage increases and converges to a maximum value ($\sim$55 V) with the increase of the resistance. The current has the opposite behaviour, converging to zero coming from a maximum value ($\sim$6 μA) reached at low resistances and finally the power

will have a maximum value ($\sim$123 μW) reached on the TENG optimal resistance (10 MΩ) and converges to zero on both sides of this maximum.

The results showed in Figures 4.10 (b) and (c), show a significant difference between the negative and positive averages of local maximum points. This difference is shown in Figures 4.9 (a) and (b), where it is observed that the negative spike goes to a higher absolute value than the positive. This happens due to the difference between the velocity that the TENG's surfaces come into contact, and the velocity they come out of contact with each other. The area of the spikes should be on average the same, this is why, another good study to do with this experimental data, would be to check the areas of the positive and negative sides of the signal, by integrating them and comparing them to check this fact.
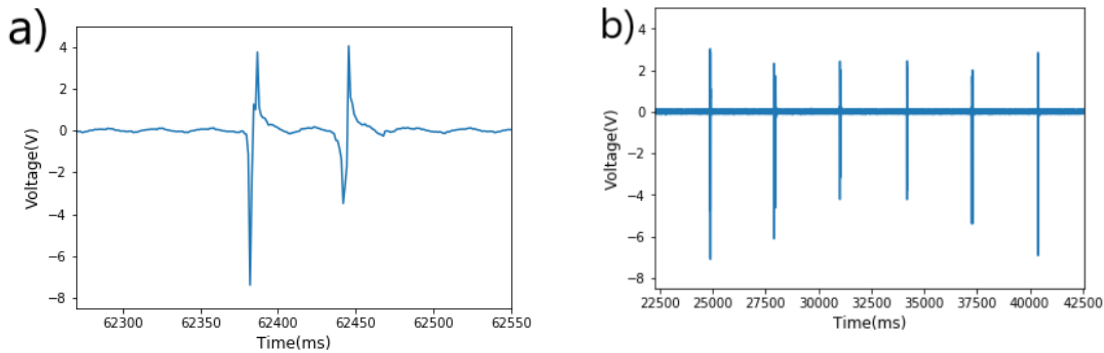
FIGURE 4.9: Raw data output of voltage with a resistance of 470 kΩ. (a) One period of motion of the LATENG and (b) Multiple periods of motion of the LATENG.

In Figure 4.9 (a) another interesting thing to observe is the two spikes within one single period. This only happend because there were 2 balls and they arrived to the LATENG, at different times, generating 2 spikes instead of 1. Finally, the last important aspect to take from Figure 4.10, is that the positive average value decreases when it gets to high resistance values. This occurs, as expected, when a contact-separation mode TENG has a high resistance, converging to an open circuit situation. This will make the voltage signal goes to zero in one of the two sides and is maximized on the other, as seen in Figure 2.9.

The resulting figures and results point the best resistance being 10 MΩ, with a 66.12 μW average absolute power output and an impressive 123.96 μW average negative power output.

4.3.2 Output dependency on the Period and Amplitude of the motion

The LATENG has the same tendencies (Figures 4.11 (a), (b) and (c)), raising its output with the increase of amplitude and decrease of period of motion, but for obvious reasons,
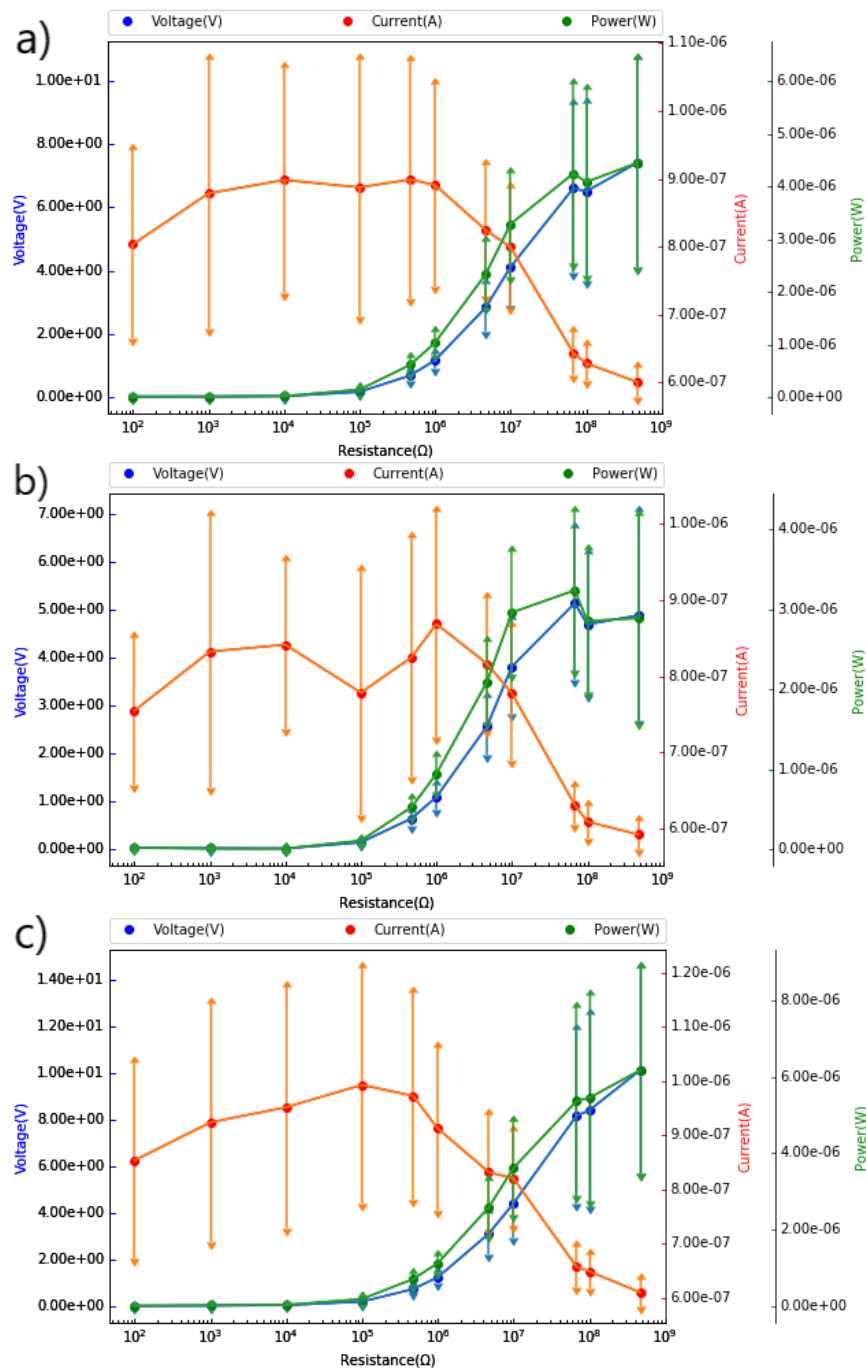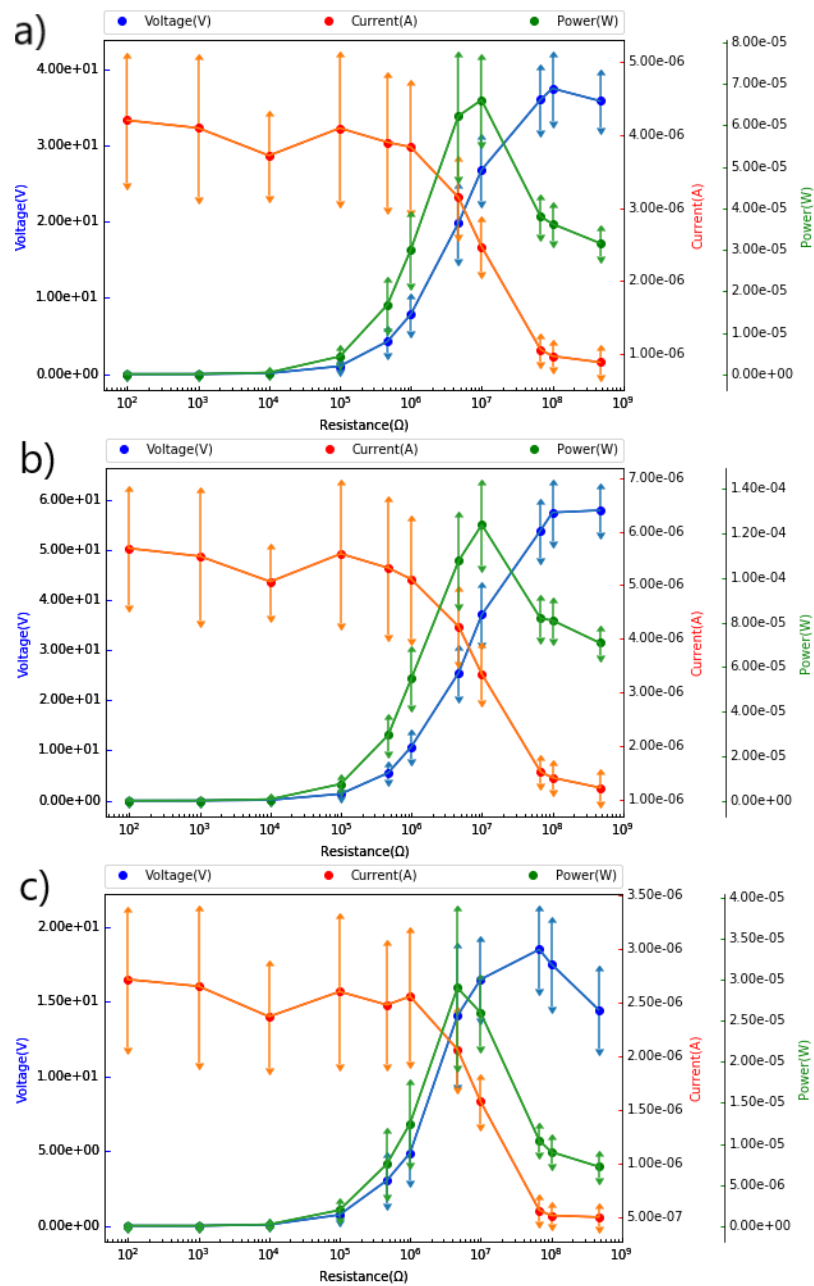
FIGURE 4.10: Average value of the local maximums for each measured quantity with a standard deviation as error bar, having the colours blue, red and green for the voltage, current and power respectively. (a) Absolute average value. (b) Negative average value. (c) Positive average value.

the amplitude looks to be more important than the period. This is because the balls need to reach one side of the structure, in order to hit the TENG.

The power output of the LATENG (Figure 4.11 (c)), at the optimal resistance, was slightly higher than the previous value (66.12 μW versus 97.59 μW). These tests were made with the same time interval as the other two, having different results, raising questions about the two different types of TENGs used and their degradation rate.
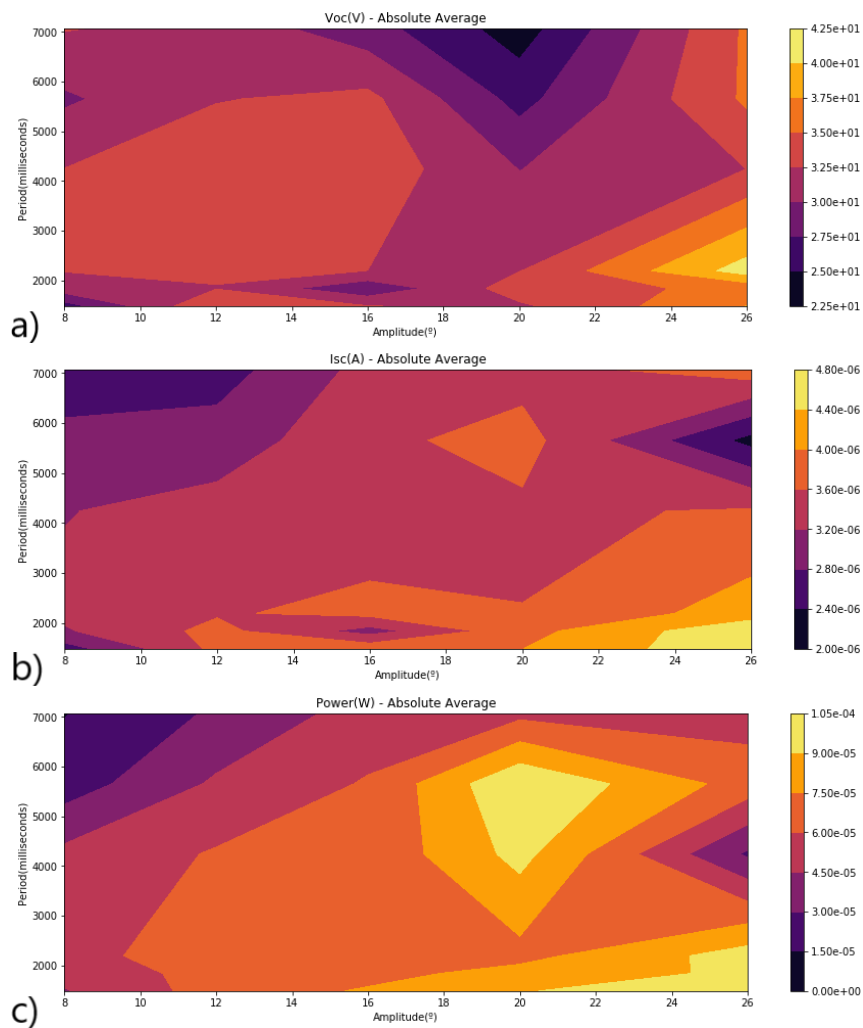
FIGURE 4.11: Results showing the dependency of multiple output quantities with different values of period and amplitude. (a) Absolute average value of V_{OC}. (b) Absolute average value of I_{SC}. (c) Absolute average value of Power with the optimal resistance for the LATENG.

4.4 Discussion and comparison of results

In the last 3 sections, the three TENGs were discussed individually. In this section a comparison between them will be done. Table 4.1 the best outputs come from the LATENG, then the ISOTENG and finally the ANISOTENG. Although the same movement was made, the nature of each TENG makes their output different from each other. This difference is larger between the LATENG and the other two TENGs, which is understandable due to their different modes of operation. A smaller difference is seen between the ISOTENG and the ANISOTENG. These have the same mode of operation and the biggest difference is that one is plane and the other has a curvature. This curvature is one of the reasons that the outputs are different, making the surfaces come into contact in a slightly

different way.

	Maximum Voltage (V)	Maximum Current (μA)	Maximum Power (μW)	Maximum Power Density (mW/m²)	Maximum Average Power (μW)	Maximum Average Power Density (mW/m²)	Degradation
ISOTENG	32,83	4,90	18,55	0,487	7,83	0,206	YES
ANISOTENG	25,50	3,05	18,04	2,097	3,28	0,381	YES
LATENG	77,41	9,93	409,98	426	66,12	68,7	NO

TABLE 4.1: Summary of the results obtain in this chapter.

Regarding the maximum power or maximum average power, a very close result for the first value is seen for the ANISOTENG and ISOTENG, but then, the second value assures the relation between the two. On the other hand, the results depending on their TENG's surface areas are much different. These show a large difference between the LATENG and the other two TENGs, and also show that the ANISOTENG has a higher output than the ISOTENG, in respect to power per TENG's area. This fact comes easy to understand, due to the different usage of area in each TENG with the movements tested. Because the axis rotates both TENGs in one way, the balls will only utilize a strip of each TENG, and with this in mind, other facts can be the determinant for these differences, like the number of balls or the curvature of the surfaces.

An important fact to take from these tests is the difference shown between the power output in the first tests of load characterisation and then (some time later) the tests of the dependency of period and amplitude. This difference for the ISOTENG and the ANISOTENG is high and cannot be explained by simple errors with the measurement at different experiment moments. As said before this does not happend with the LATENG, creating the idea that the origin for this difference is the mode how the TENGs operate. This mode depends on the wrinkles on the surface of the TENG, which creates differences on the distances between the TENG's surfaces and, when the balls pass above, they make the opposite surfaces come into contact and generate energy. On the other hand, the LATENG does not need this wrinkles on its surfaces, having its output more dependent on the degradation of the surfaces of the TENG itself, instead of the surfaces wrinkles. This opens the possibility to predict that the wrinkles of the surface with a small amount of time will be smoothed out and make the ISOTENG and ANISOTENG output's decrease. In the case of the LATENG, the surfaces of the TENG should behave as the second

phase of the other two TENGs, taking long periods of time to decrease its output values.

Finally, some other optimizations to do should be, for example, to understand in each TENG, what would be the best amount of balls and surface curvature, use more resistances in the zone where the optimal resistance is located or the angle that the LATENG uses between the dynamic and the locked surface.

In the next chapter, the way the TENGs behave over time will be experimentally studied, building a new structure to hold multiple TENGs at the same time, fabricating new TENG surfaces, building new testing software and new processing software for this degradation experiment.

Chapter 5

Degradation of TENGs throughout time

A general fact acquired with the previous chapter was that two of the three TENGs tested had a decreasement of the output power throughout time. This was the motivation to follow the work of this dissertation into experimental tests to understand how and how long it takes for TENGs to decrease their output by a certain percentage. For these experimental tests, a new structure was built, with a more reliable and durable motor for the axis rotation, an attached *Switcher* board, to switch between TENGs and an upgraded version of the homemade LABVIEW program used previously in this dissertation.

5.1 One direction test structure for multiple TENGs degradation experimental tests

The goal for this chapter is to experimentally understand how different types of TENGs diminish their output with time. For this, a long period of testing time is needed for each TENG to have a good understanding of their degradation behaviour. This was the reason for the building of a new structure that also allowed to perform a single test of degradation with three TENGs at the same time. This single test will be possible because a *Switcher* board was developed and built for this purpose. The board will have the task of connecting each of the three TENGs independently and outputting a single selected TENG at a time for the electrometer measurement connection. This selection will be possible because in the board there is an 8-bit shift register (SN74HC595) that selects one

out of eight possible solid-state relays, which are connected with the output of one of the TENGs tested.

The schematic layout can be observed in Appendix C and, in Figure 5.1 (a), a picture of the board layout can be seen. Figure 5.1 (b) shows the board with 4 possible outputs in the top section (numbered 1), as this was the necessary number for these tests. The number 2 in the figure shows the connections made with the Arduino Uno to control the selection of the output and the number 3 shows the output wires to the TENGs.
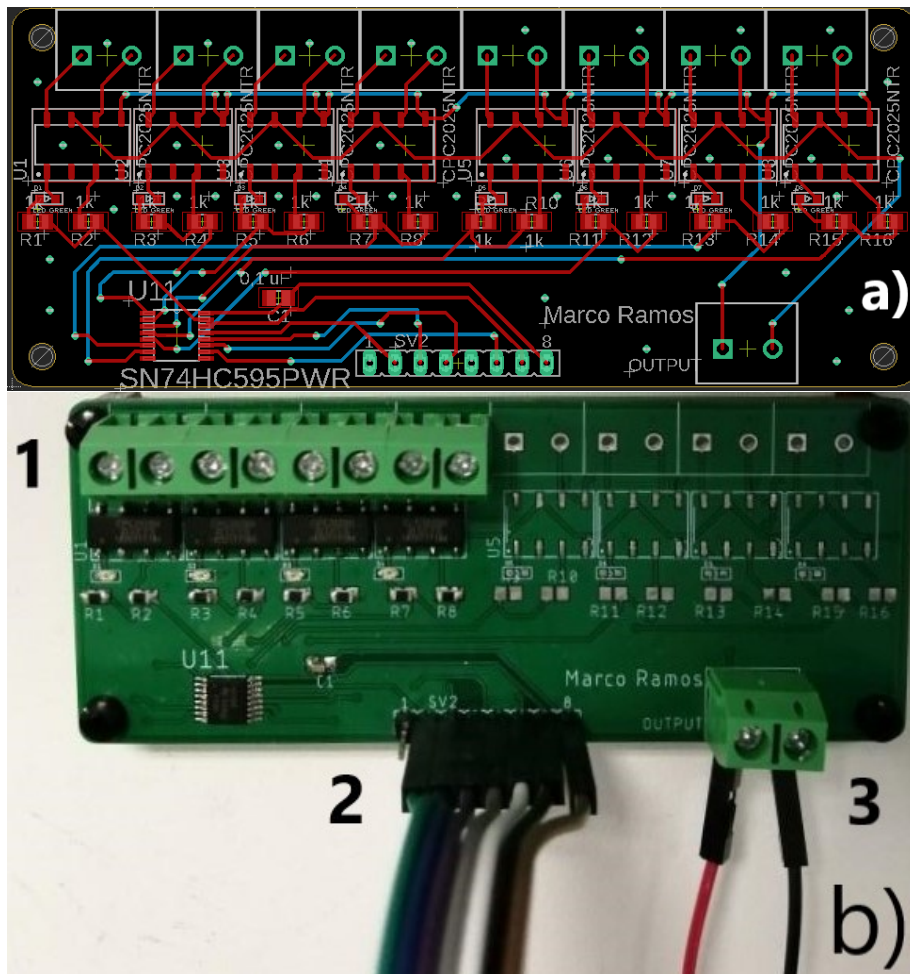
FIGURE 5.1: (a) Board layout of the Switcher Board and (b) *Switcher* Board used in the TENGs degradation tests.

The electrometer measurement will be performed as in the last chapter and no modification were required. However, unlike the electrometer, the LABVIEW program had to be changed. This was related with the number of cycles to be performed and the number of TENGs tested, so that the program had to send a serial message to the Arduino to select each TENG in the *Switcher* board.
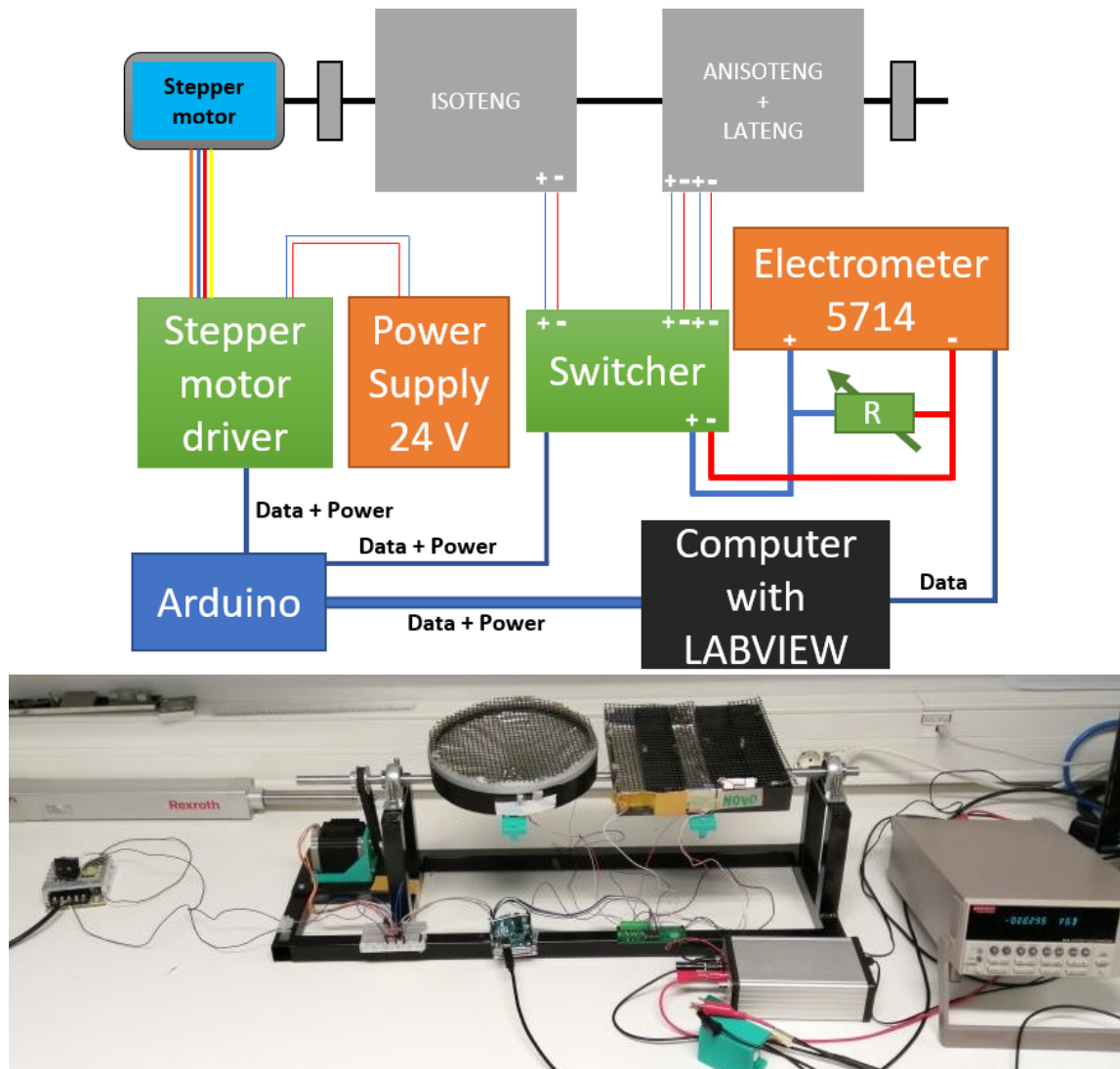
FIGURE 5.2: One direction test structure for multiple TENGs degradation experimental tests (a) Illustration of the complete setup and (b) Picture of the setup without showing the computer used to safe and acquire data.

One last part needed for this degradation tests will be the use of a stronger motor instead of the servomotor utilized in the first setup. This new motor is a stepper motor (103H7126-5740 [39]) with much larger values of torque, steps of 1.8 degrees and for its control an A4988 driver is used. This motor also requires a power supply voltage of 24 V. The reason for this change was the unreliability of the previously used servomotor for long term tests like the ones intended here.

Finally, the complete system is illustrated in Figure 5.2 (a) and the most important components can be seen in Figure 5.2 (b). This system will be used in a degradation test with the three prototype TENGs tested at the same time and will take several days to show relevant results, resulting on a large amount of data to be saved and processed.

5.2   Results of the degradation tests

In order to achieve good results and observable tendencies, the duration of the degradation tests will be very long (over 12 days). Each TENG will be measured for 5 minutes in a sequence, achieving a 5 minute period of measurement per TENG and 15 minutes of total testing time per cycle. This results in four data sets (average of the 5 minute measurement) every hour and 96 every day per TENG. Also, after 9 days of continuous movement, the experiment had to be paused for 36 hours due to an electrical power down for maintenance purposes at FCUP. After these tests were finished, the acquired data of each TENG was processed. The following subsections will address these results separately for each TENG.

5.2.1   ISOTENG

The ISOTENG shows a clear behaviour of the output throughout time (Figure 5.3 (a)). This behaviour shows an increasing of the output in the beginning of the test period (up to 14.2 V and 9.5 hours of testing). This raising behaviour should be due to the accumulation of charges on the surface of the prototype. Because the surface used by the balls is big, this maximum will take time to be reached. After this maximum value is reached, the output starts converging continuously to a much lower value than the maximum. When the ANISOTENG reaches this zone (after ~24 hours), the average decreasing of the output will be very low, having some pseudo-periodic wave-like behaviour.

The primary behaviour showed was expected, with a fast degradation of the output in the beginning of the experimental test and slower after some days showing a linear decreasing of the output. The fast degradation phase is easy to understand in this prototype. Observing Figure 5.4 (taken after the tests), it is obvious that the TENG layers are damaged and completely joined together in most of the path used by the moving balls, leading us to conclude that this is the reason for the fast degradation seen in the beginning.

The wave-like behaviour seen in Figure 5.3 (b), should have a reasonable explanation, being most likely because large temperature differences between day and night and also because the lab where the experimental test was done was directly exposed to sunlight on the afternoon, making the values of voltage increase even more during that period. In fact, the zones where the periodic maximums appear are between 4 and 7 pm and this is the time where the local temperature at the setup is higher.

FIGURE 5.3: Absolute maximums average of the V_{OC} of the ISOTENG throughout time (a) Total experimental period and (b) Focus on wave-like pseudo-periodic behaviours.

FIGURE 5.4: State of the ISOTENG after the degradation test.

5.2.2 ANISOTENG

The ANISOTENG shows a similar tendency of the output through time (Figure 5.5 (a)). In this case, the behaviour shows the same increase of the output in the beginning of the test period, but the maximum value is reached slightly earlier (up to 7.2 V and 1.5 hours of testing). This raising behaviour should also be due to the accumulation of charges at the surface of the prototype. Because the surface used by the balls is smaller than the ANISOTENG surface, this maximum will take less time to be reached and the rate that this surfaces degrade will be slower. The output starts converging continuously to a lower value compared with the initial and the maximum reached. If we ignore these initial points, the behaviour of the degradation looks like an exponential function with a positive base smaller than one, converging to a value which in this case is ~3 V. Also, the zones with two vertical blue lines relate to broken connection of the prototype with the *Switcher* board that had to be redone in real time.

FIGURE 5.5: Absolute maximums average of the V_{OC} of the ANISOTENG throughout time (a) Total experimental period and (b) Focus on wave-like pseudo-periodic behaviours.

After more time than tested, the output voltage of the prototype should start lowering

even more, but this should be very slow and due to the movements of the balls above the TENG layers, damaging the silver layer under the moving balls and the TENG layers inside the prototype. Another thing that can be the reason for the slower degradation is the use of only 2 steel balls, instead of 6 or 10 as in the ISOTENG.

In Figure 5.5 (b), a similar pseudo-periodic wave-like behaviour is observed and for the same reasons as the ISOTENG. Then again, these periodic maximums appear between 4 and 7 pm related with the temperature increase of the laboratory by direct sunlight exposure.

The slow degradation phase is understandable. By observing Figure 5.6, it is obvious that the TENG layers are partially joined together in most of the path used by the moving balls, concluding that, in the future, this output can get even lower.

FIGURE 5.6: State of the ANISOTENG after the degradation test.

At the end of the tests, as Figure 5.6 shows, the ISOTENG does not present the same degradation on the surfaces as the ANISOTENG, possibly coming from two reasons. The first reason is the quantity of steel balls, which is smaller in the ANISOTENG case, resulting in a slower degradation rate than the ISOTENG with a larger number of steel balls. The second reason can come from the curvature difference between the two prototypes.

5.2.3   LATENG

The last prototype to be studied shows a general tendency different from the other prototypes studied. In the LATENG case, we see a general tendency of increasing output with time, reaching a zone where we see the pseudo-periodic wave-like behaviour (due to the temperature variations). This will result on these periodic maximums (Figure 5.7 (b)) appearing at the same times as the periodic maximums of other two prototypes. Then again, the zones with two vertical blue lines are where the connection of the prototype with the *Switcher* board was damaged.
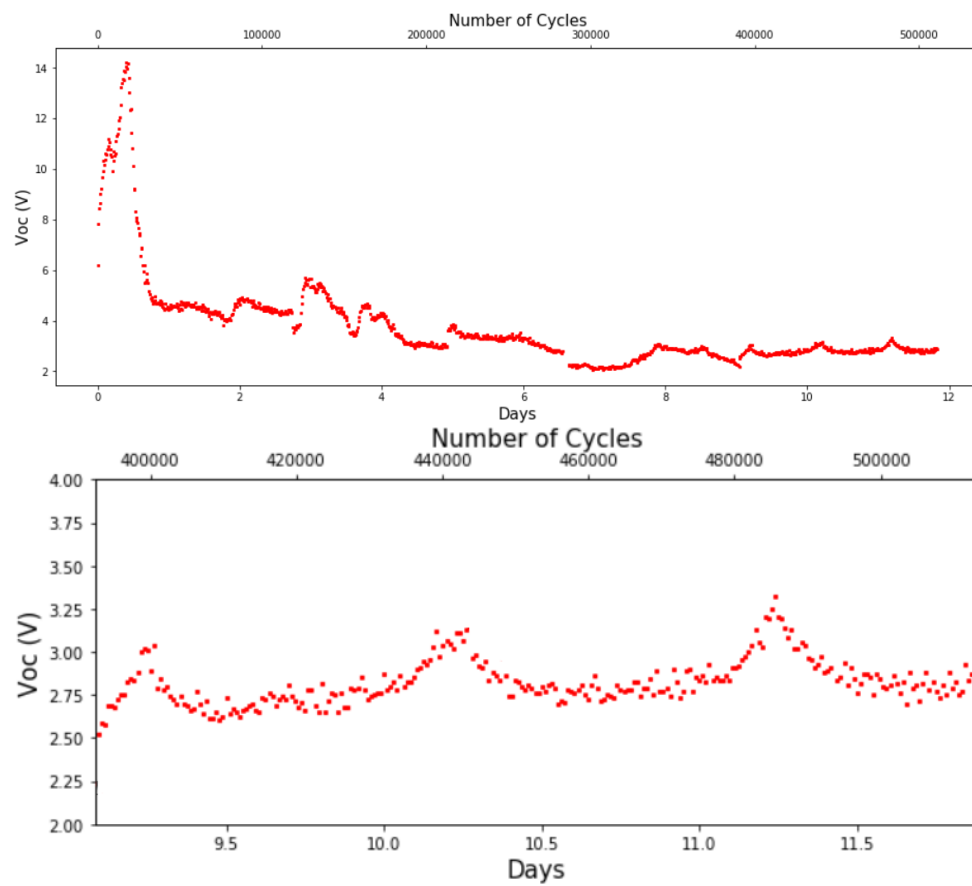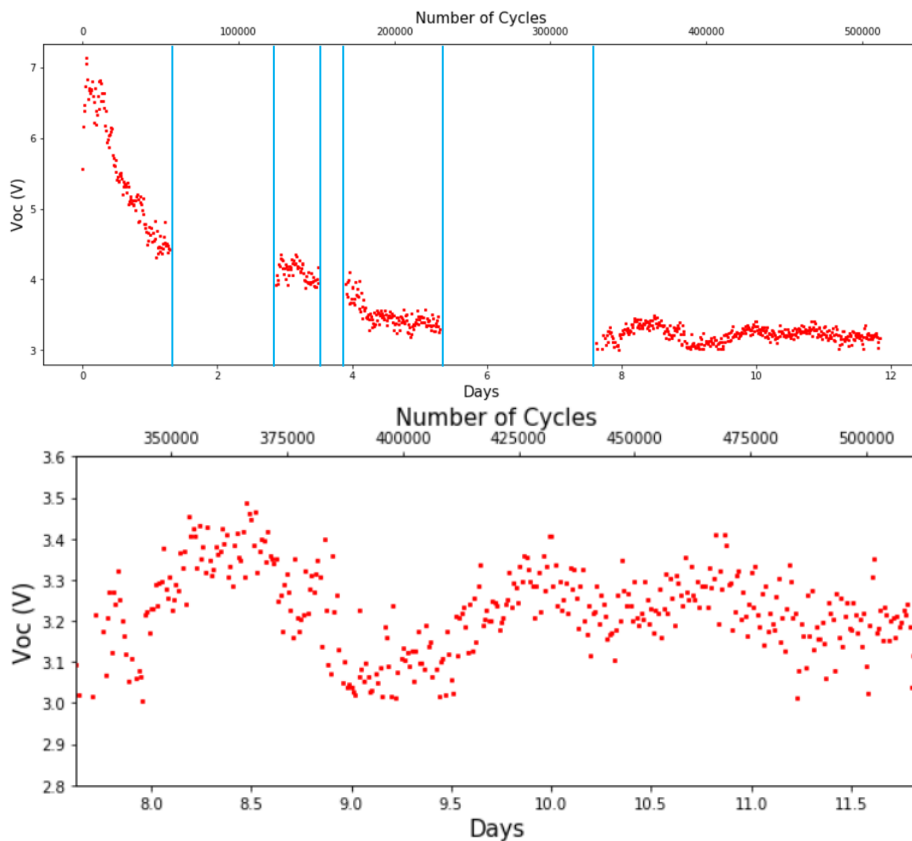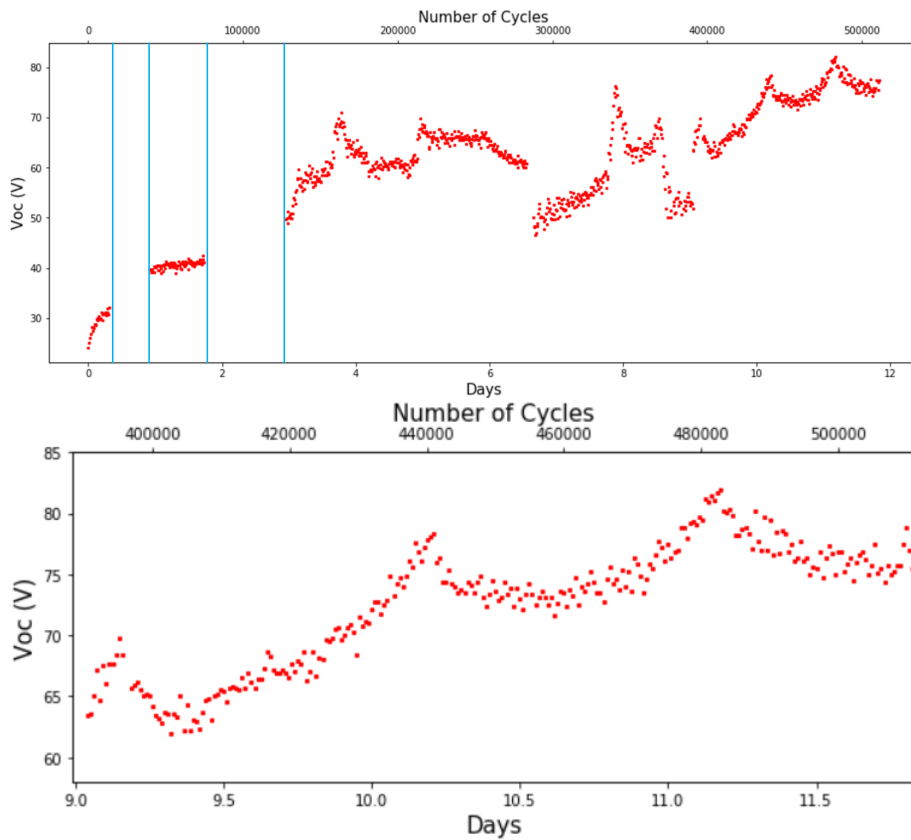
FIGURE 5.7: Positive maximums average of the V_{OC} of the LATENG throughout time
(a) Total experimental period and (b) Focus on wave-like pseudo-periodic behaviours.

In Figure 5.7, instead of the absolute average being used, the positive average was used. This was due to the large difference showed between the positive and negative spikes in this prototype on the contrary of the other prototypes.

The large difference between the output of this prototype throughout time compared with the other two comes mainly from the difference between their mode of energy generation and structure. In the case of the LATENG, no layers are needed to be put on top of the other, the two triboelectric layers are plane and do not depend on change in their wrinkles throughout time, resulting in a different degradation behaviour. The general behaviour showed the output increasing slowly with time, but with this experimental period it is possible to predict that with more testing time, the output would enter in a zone where it would decrease slowly due to the degradation of the triboelectric materials.

5.3   Discussion

The ISOTENG and ANISOTENG show similar degradation behaviours with an initial large dependency on the wrinkles of their surfaces and only later in the experimental period show truly their triboelectric layers degradation. The LATENG, on the other hand, shows few indications of degradation of its triboelectric layers within this experimental period, being possible that with a larger testing period this could be observable experimentally. In general, all prototypes show some pseudo-periodic wave-like behaviours that is likely temperature dependent [40] [41]. If another degradation experimental test would be possible, one should consider varying the testing period, that should be increased, and enhancing the robustness of the connections of the prototypes wires with the *Switcher* board.

Chapter 6

Conclusion and Future work

6.1 Conclusion

One of the main goals for this dissertation was the automation of the processing of data from triboelectric nanogenerators. Before the software tool developed in this dissertation, this task of processing data from TENGs would need a large amount of hours of work for students or researchers. Now with a few clicks the results are generated and verified. Although this software tool was important, the results processed with this tool were also very important.

First, the characterization of the optimal load resistances of three different TENGs for the blue energy harvesting was performed, with all of these TENGs having a optimal resistance of 10 MΩ. Another study was performed on the dependence of the amplitude and period of the motion made by the TENGs, enabling the understanding on how these are important for the output of these different prototypes. The clear result from these tests was that with the increase of amplitude and decrease of period the output generally increases.

One clear problem was observed in between these two studies, a clear degradation was happening with at least 2 out of the 3 TENGs. This problem was the leading factor into studying degradation effects in TENGs as a next step in this dissertation. The results of this study of the degradation of TENGs was that the ANISOTENG and ISOTENG initially showed a behaviour in which their output voltage decreased greatly due to the loss of wrinkles on the upper surfaces. After some time, both entered a phase where the output voltage decrease slowed down to a baseline, with some fluctuations due to temperature differences during the day. In the case of the LATENG, in the beginning it

showed a slight output voltage increase untill it reached the same baseline behaviour as the other two TENGs with the same fluctuations due to temperature differences.

6.2   Future work

Some improvements can be made to the software tool and both systems created in this dissertation. The first, for a faster processing time and the second for problems like the ones seen in the degradation tests, improving the quality of the connections as a prevention on tests with a long experimental period. Finally, one last improvement for a future testing structure would be the increasement of degrees of freedom, for example, having more than one axis of rotation for a better ocean wave imitation.

6.2.1   Bi-dimensional test structure for TENGs experimental tests

In the both setups developed before in this dissertation, one thing to improve was the number of degrees of freedom of the axis of rotations. Given the importance of the pitch and roll motion, instead of having only one axis of rotation, to make the wave simulation more realistic, one should add another rotation axis. Also, the acquisition was made with an electrometer which is expensive and heavy, so an alternative method would be interesting for a new setup. Such new setup should have a bi-dimensional test structure to simulate ocean waves for TENG experimental tests. During dissertation we started already the implementation of a bi-dimensional design using two simple servomotors to move the axis of rotation. The servomotors were controlled with an Arduino Uno with a code developed together with Isabel Gonçalves (MIEF student) similar to the Appendix B but for 2 axis at the same time. This Arduino was connected to a Raspberry Pi (RP) by USB serial communication, having this RP the task to control the whole acquisition and the movement of the servo motors all at the same time. Also, the RP was connected with a Touch Screen by a HDMI cable to show the data in real time. The RP will acquire data from two parameters in this setup. The first is the rotational movements of the two axis of rotation and the second is the output voltage and current of the TENG itself. The acquisition of the rotational movements is done with the help of a small gyroscope (MPU6050 [42]) that communicates with the RP by I^{2}C protocol.

The output voltage and current acquisition is made with the help of an acquisition board developed by Ricardo Esteves (InanoEnergy). This board has 2 functions, the first

is the selection of the load resistance for the TENG and the second is the acquisition of the
voltage and current from the TENG. The selection of the resistance is made by the Arduino
Uno that is controlled by the RP to change the selected resistance. Finally, the acquisition
is made with the help of an Analog-to-digital converter (ADS1115 [43]) controlled by the
RP with I^{2}C protocol. The data from the gyroscope and the acquisition board is plotted
in real time on the touch screen enabling any problem to be solved without the need to
process the data after acquiring it.
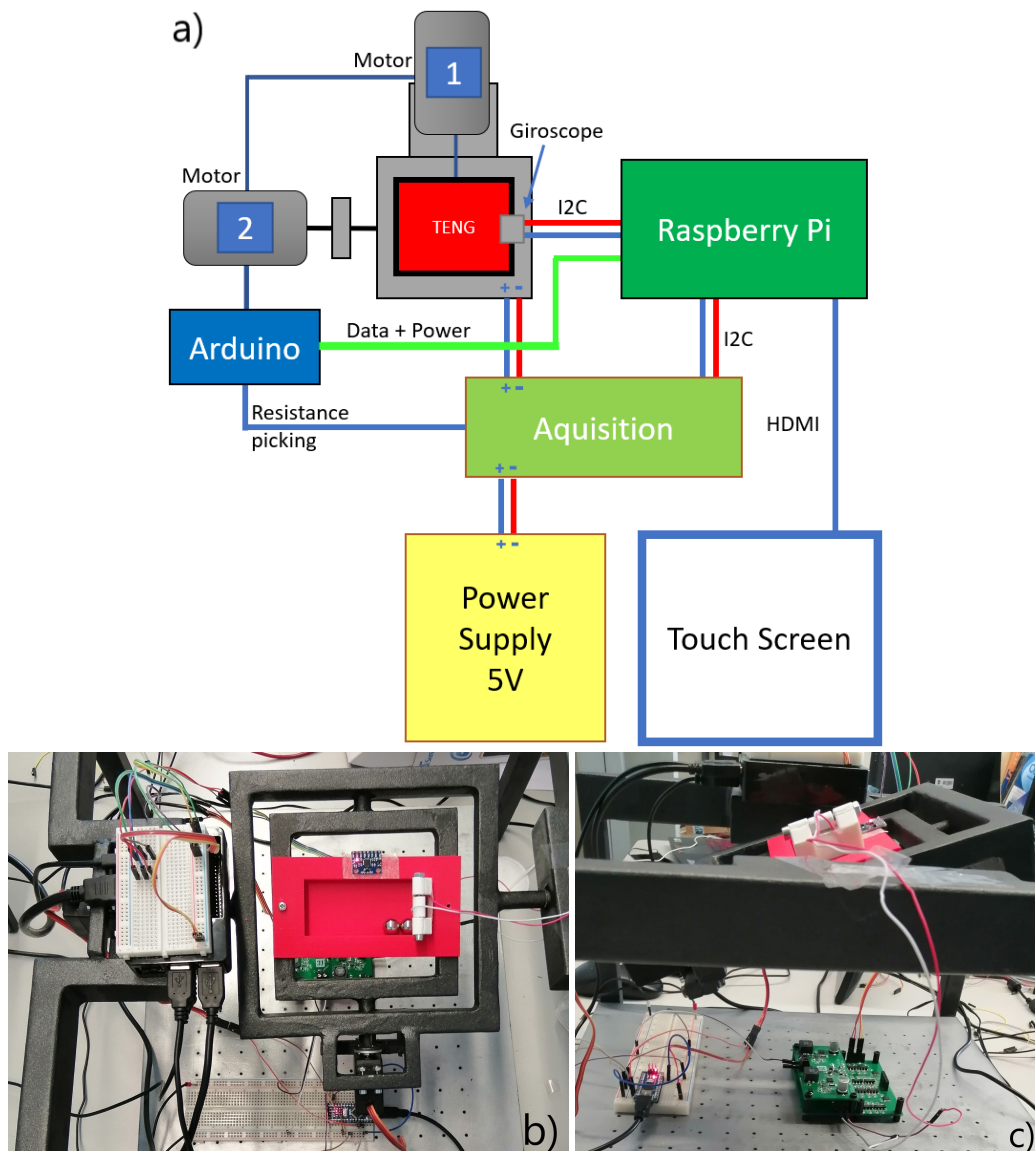
FIGURE 6.1: (a) Illustration of the new setup, (b) Top view of the new setup and (c) Lateral
view of the new setup

Figure 6.1 (a) shows , an illustration of the complete setup and connections. In Figure
6.1 (b), a picture of a top view of the bi-dimensional system is showed. In that figure we

can see, on the left, the Raspberry Pi and, on the right, both axis joined with the TENG in the middle and on the top of it the gyroscope. Finally, in Figure 6.1 (c) a lateral view of the setup is shown, with both axis on the top and the Arduino Uno and the acquisition board underneath.

The acquired data with this setup can then be processed by the software tool created in this dissertation creating the required plots to visualize the experimental results as necessary.

Appendix A

Servomotor Arduino code used to move with a specific amplitude and period

```
1  #include <Servo.h>
   Servo myservo;  // create servo object to control a servo
3  //------------Change only these first 3 values----------------
   int Initial = -13;  // Initial relative angle
5  int Final = 13;     // Final relative angle
   int Period = 1486; // Period of motion in ms
7  //--------------------------------------------------------
   int AInicial = 76 + Initial;  // initial absolute angle
9  int AFinal = 76 + Final;      // final absolute angle
   int total = Final - Initial;  // total angle
11 int angulo = 0;                    // variable to store the servo position
   double Delay = 0;                  // variable to store the delay value
13
   void setup() {
15   Delay =(double) Period/(2*total); // delay for each step.
     myservo.attach(9);                   // attaches the pin 9 to the servo
17 }
   void loop() {
19   for (angulo = AInicial; angulo <= AFinal; angulo += 1) {// Initial --> Final
       myservo.write(angulo); // tell servo to go to position in variable 'angulo'
```

```
21     delay(Delay); }           // make a small delay between steps
     for (angulo = AFinal; angulo >= AInicial; angulo -= 1) {// Final --> Initial
23     myservo.write(angulo); // tell servo to go to position in variable 'angulo'
       delay(Delay);}            // make a small delay between steps
25 }
```

Appendix B

Servomotor Arduino code used on the study with different values for amplitude and period of motion

```
1  #include <Servo.h>
   Servo myservo;  // create servo object to control a servo
3  int myPeriods[6] = {1486,1840,2194,4243,5657,7071}; // array with periods used
   int myAmplitudes[5] = {4,6,8,10,13}; // array with half amplitudes used
5  //------------------------------------------------
   int angulo = 0;      // variable to store the servo position
7  double Delay = 0;    // variable to store the delay value
   int Period = 0;      // Period of motion in ms
9  int Amplitude = 0;   // Amplitude in degrees
   int AInicial = 0;    // initial angle
11 int AFinal = 0;      // final angle
   int total = 0;       // total normal of angles
13 int iPeriod = 0;     // integer for period
   int iAmplitude = 0;  // integer for amplitude
15 int index = -1 ;     // counting variable
   uint8_t index_aux = 0;

17

   void setup() {
19   myservo.attach(9);  // attaches the servo on pin 9 to the servo
     Serial.begin(9600); // start communication
```

```
21    pinMode(LED_BUILTIN, OUTPUT);
   }
23  void loop() {
     myservo.write(76); // to start at the initial angle
25    if (Serial.available()){
       digitalWrite(LED_BUILTIN, HIGH); //turn led on
27      index_aux = Serial.read(); // reads the byte sent from the labview program
       index = index +1;
29      iPeriod = index%6; // integer
       iAmplitude= index/6; // rest division
31      Period = myPeriods[iPeriod]; // period of motion
       Amplitude = myAmplitudes[iAmplitude]; // 1 angle to each side
33      AInicial = 76 - Amplitude; // initial angle
       AFinal = 76 + Amplitude;   // final angle
35      Delay = (double)Period/(2*Amplitude); // delay for each step.
     }
37    if (index >= 0){
       for (angulo = AInicial; angulo <= AFinal; angulo += 1) { // steps of 1 degree
        - going from initial to the final angle
39        myservo.write(angulo); //go to position in variable 'angulo'
         delay(Delay);         // make a small delay between steps
41       }
       for (angulo = AFinal; angulo >= AInicial; angulo -= 1) { // steps of 1 degree
        - going from final to the initial angle
43        myservo.write(angulo); //go to position in variable 'angulo'
         delay(Delay);          // make a small delay between steps
45       }
     }
47    digitalWrite(LED_BUILTIN, LOW);  //turn led off
   }
```
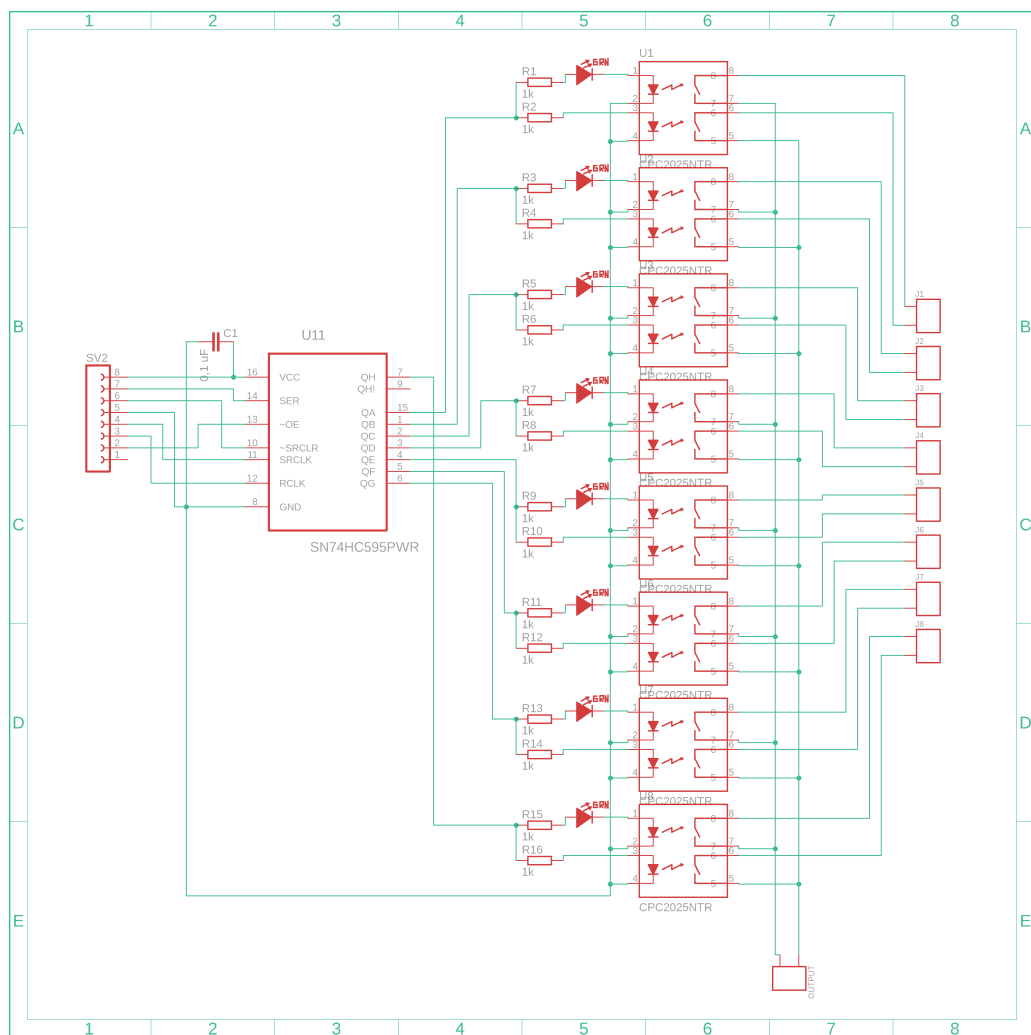
Appendix C

Schematic of the *Switcher* board used on the degradation tests

Bibliography

[1] C. Maduko and U. Akuru, "Future trends on global energy demand," 07 2013.

[2] T. Fossum, "Intelligent autonomous underwater vehicles a review of auv autonomy and data-driven sample strategies," 09 2016.

[3] C. Albaladejo, P. Sanchez, A. Iborra, F. Soto, J. López, and R. Torres, "Wireless sensor networks for oceanographic monitoring: A systematic review," *Sensors (Basel, Switzerland)*, vol. 10, pp. 6948–68, 07 2010.

[4] N. Sharma, J. Gummeson, D. Irwin, and P. Shenoy, "Cloudy computing: Leveraging weather forecasts in energy harvesting sensor systems," *Proc. SECON*, pp. 1–9, 01 2010.

[5] Z. Wang, L. Lin, S. Niu, and Y. Zi, *Triboelectric Nanogenerators*, 01 2016.

[6] K. Tao, H. Yi, Y. Yang, H. Chang, J. Wu, L. Tang, Z. Yang, N. Wang, L. Hu, Y. Q. R. Fu, J. Miao, and W. Yuan, "Origami-inspired electret-based triboelectric generator for biomechanical and ocean wave energy harvesting," *Nano Energy*, 10 2019.

[7] C. Rodrigues, C. Alves, J. Puga, A. Pereira, and J. Ventura, "Triboelectric driven turbine to generate electricity from the motion of water," *Nano Energy*, vol. 30, 10 2016.

[8] K. Lee, J.-W. Lee, K. Kim, D. Yoo, D. Kim, W. Hwang, I. Song, and J.-Y. Sim, "A spherical hybrid triboelectric nanogenerator for enhanced water wave energy harvesting," *Micromachines*, vol. 9, p. 598, 11 2018.

[9] "Engineering materials at the nanoscale for triboelectric nanogenerators," *Cell Reports Physical Science*, p. 100142, 08 2020.

[10] "Toward the blue energy dream by triboelectric nanogenerator networks," *Nano Energy*, vol. 39, pp. 9 – 23, 2017. [Online]. Available: http://www.sciencedirect.com/science/article/pii/S2211285517303890

[11] P. Iversen and D. Lacks, "A life of its own: The tenuous connection between thales of miletus and the study of electrostatic charging," *Journal of Electrostatics*, vol. 70, p. 309–311, 06 2012.

[12] S. Pan and Z. Zhang, "Fundamental theories and basic principles of triboelectric effect: A review," *Friction*, vol. 7, 08 2018.

[13] F.-R. Fan, Z.-Q. Tian, and Z. L. Wang, "Flexible triboelectric generator," *Nano Energy*, vol. 1, no. 2, pp. 328 – 334, 2012. [Online]. Available: http://www.sciencedirect.com/science/article/pii/S2211285512000481

[14] Z. L. Wang, "Triboelectric nanogenerators as new energy technology for self-powered systems and as active mechanical and chemical sensors," *ACS Nano*, vol. 7, no. 11, pp. 9533–9557, 2013.

[15] L. Zheng, Z.-H. Lin, G. Cheng, W. Wu, X. Wen, S. Lee, and Z. L. Wang, "Silicon-based hybrid cell for harvesting solar energy and raindrop electrostatic energy," *Nano Energy*, vol. 9, pp. 291 – 300, 2014. [Online]. Available: http://www.sciencedirect.com/science/article/pii/S2211285514001736

[16] H. Zou, Y. Zhang, L. Guo, P. Wang, X. He, G. Dai, H. Zheng, C. Chen, A. Wang, C. Xu, and Z. Wang, "Quantifying the triboelectric series," *Nature Communications*, vol. 10, 12 2019.

[17] S. Gauntt, G. Batt, and J. Gibert, "Dynamic modeling of triboelectric generators using lagrange's equation," p. V001T07A009, 09 2017.

[18] C. Rodrigues, D. Nunes, D. Clemente, N. Mathias, J. M. Correia, P. Rosa-Santos, F. Taveira-Pinto, T. Morais, A. Pereira, and J. Ventura, "Emerging triboelectric nanogenerators for ocean wave energy harvesting: state of the art and future perspectives," *Energy Environ. Sci.*, pp. –, 2020. [Online]. Available: http://dx.doi.org/10.1039/D0EE01258K

[19] L. McCarty and G. Whitesides, "Electrostatic charging due to separation of ions at interfaces: Contact electrification of ionic electrets," *Angewandte Chemie (International ed. in English)*, vol. 47, pp. 2188–207, 02 2008.

[20] C. Xu, B. Zhang, A. C. Wang, H. Zou, G. Liu, W. Ding, C. Wu, M. Ma, P. Feng, Z. Lin, and Z. L. Wang, "Contact-electrification between two identical materials: Curvature effect," *ACS Nano*, vol. 13, no. 2, pp. 2034–2041, 2019.

[21] F. Fan, L. Lin, G. Zhu, W. Wu, R. Zhang, and Z. Wang, "Transparent triboelectric nanogenerators and self-powered pressure sensors based on micropatterned plastic films," *Nano letters*, vol. 12, pp. 3109–14, 05 2012.

[22] I.-W. Tcho, W.-G. Kim, S.-B. Jeon, S.-J. Park, B. J. Lee, H.-K. Bae, D. Kim, and Y.-K. Choi, "Surface structural analysis of a friction layer for a triboelectric nanogenerator," *Nano Energy*, vol. 42, pp. 34 – 42, 2017. [Online]. Available: http://www.sciencedirect.com/science/article/pii/S2211285517306420

[23] S. Niu and Z. Wang, "Theoretical systems of triboelectric nanogenerators," *Nano Energy*, vol. 14, 11 2014.

[24] S. Shafeek, "Theoretical and numerical analysis of triboelectric nanogenerators for self-powered sensors," 12 2016, pp. 1–4.

[25] S. Niu, S. Wang, L. Lin, Y. Liu, Y. S. Zhou, Y. Hu, and Z. L. Wang, "Theoretical study of contact-mode triboelectric nanogenerators as an effective power source," *Energy Environ. Sci.*, vol. 6, pp. 3576–3583, 2013. [Online]. Available: http://dx.doi.org/10.1039/C3EE42571A

[26] H. Zhang, Y. Lu, A. Ghaffarinejad, and P. Basset, "Progressive contact-separate triboelectric nanogenerator based on conductive polyurethane foam regulated with a bennet doubler conditioning circuit," *Nano Energy*, vol. 51, 06 2018.

[27] G. Zhu, C. Pan, W. Guo, C.-Y. Chen, Y. Zhou, R. Yu, and Z. Wang, "Triboelectric-generator-driven pulse electrodeposition for micropatterning," *Nano letters*, vol. 12, pp. 4960–5, 08 2012.

[28] S. Niu, Y. Liu, S. Wang, L. Lin, Y. Zhou, Y. Hu, and Z. Wang, "Theory of sliding-mode triboelectric nanogenerators," *Advanced materials (Deerfield Beach, Fla.)*, vol. 25, 11 2013.

[29] ——, "Theoretical investigation and structural optimization of single-electrode triboelectric nanogenerators," *Advanced Functional Materials*, vol. 24, 06 2014.

[30] S. Niu, Y. Liu, X. Chen, S. Wang, Y. S. Zhou, L. Lin, Y. Xie, and Z. L. Wang, "Theory of freestanding triboelectric-layer-based nanogenerators," *Nano Energy*, vol. 12, pp. 760 – 774, 2015. [Online]. Available: http://www.sciencedirect.com/science/article/pii/S2211285515000142

[31] R. de Winter, "Designing ships using constrained multi-objective efficient global optimization," 05 2018.

[32] M. Xu, T. Zhao, C. Wang, S. Zhang, X. Pan, and Z. Wang, "High power density tower-like triboelectric nanogenerator for harvesting arbitrary directional water wave energy," *ACS Nano*, vol. 13, 01 2019.

[33] S. Zhang, M. Xu, C. Zhang, Y.-C. Wang, H. Zou, X. He, Z. Wang, and Z. Wang, "Rationally designed sea snake structure based triboelectric nanogenerators for effectively and efficiently harvesting ocean wave energy with minimized water screening effect," *Nano Energy*, vol. 48, 03 2018.

[34] P. Cheng, H. Guo, C. Zhang, X. Yin, X. Li, D. Liu, W. Song, X. Sun, J. Wang, and Z. Wang, "Largely enhanced triboelectric nanogenerator for efficient harvesting of water wave energy by soft contacted structure," *Nano Energy*, vol. 57, 12 2018.

[35] F. Xi, Y. Pang, G. Liu, S. Wang, W. Li, C. Zhang, and Z. Wang, "Self-powered intelligent buoy system by water wave energy for sustainable and autonomous wireless sensing and data transmission," *Nano Energy*, vol. 61, 04 2019.

[36] A. Ahmed, Z. Saadatnia, I. Hassan, Y. Zi, Y. Xi, X. He, J. Zu, and Z. L. Wang, "Self-powered wireless sensor node enabled by a duck-shaped triboelectric nanogenerator for harvesting water wave energy," *Advanced Energy Materials*, vol. 7, no. 7, p. 1601705, 2017. [Online]. Available: https://onlinelibrary.wiley.com/doi/abs/10.1002/aenm.201601705

[37] Z. Saadatnia, E. Asadi, H. Askari, J. Zu, and E. Esmailzadeh, "Modeling and performance analysis of duck-shaped triboelectric and electromagnetic generators for water wave energy harvesting," *International Journal of Energy Research*, vol. 41, 07 2017.

[38] K. a Tektronix Company, "Model 6514 system electrometer instruction manual." [Online]. Available: https://www.tek.com/low-level-sensitive-and-specialty-instruments/high-resistance-low-current-electrometers-series-650-5

[39] S. D. Global. [Online]. Available: https://www.sanyodenki.com/archive/document/product/servo/catalog_E_pdf/SANMOTION_F2_E.pdf

[40] C. X. Lu, C. B. Han, G. Q. Gu, J. Chen, Z. W. Yang, T. Jiang, C. He, and Z. L. Wang, "Temperature effect on performance of triboelectric nanogenerator," *Advanced Engineering Materials*, vol. 19, no. 12, p. 1700275, 2017. [Online]. Available: https://onlinelibrary.wiley.com/doi/abs/10.1002/adem.201700275

[41] M. Olsen, J. Ortegren, R. Zhang, S. Reza, H. Andersson, and H. Olin, "Schottky model for triboelectric temperature dependence," *Scientific Reports*, vol. 8, p. 5293, 03 2018.

[42] TDK. [Online]. Available: https://invensense.tdk.com/products/motion-tracking/6-axis/mpu-6050/

[43] TI. [Online]. Available: https://www.ti.com/lit/ds/sbas444d/sbas444d.pdf?ts=1599009105851&ref_url=https%253A%252F%252Fwww.google.com%252F